Check for updates

Retrieval of Martian atmospheric CO vertical profiles from NOMAD observations during the 1st year of TGO operations

Ashimananda Modak[1], Miguel Angel López-Valverde[1], Adrian Brines[1], Aurélien Stolzenbach[1], Bernd Funke[1], Francisco González-Galindo[1], Brittany Hill[1], Shohei Aoki[3], Ian Thomas[2],Giuliano Liuzzi[4,5], Gerónimo Villanueva[4], Justin Erwin[2], José Juan Lopez Moreno[1], Nao Yoshida[12], Udo Grabowski[8], Francois Forget[13], Frank Daerden[2],Bojan Ristic[2],Giancarlo Bellucci[10], Manish Patel[11], Loic Trompet[2], and Ann-Carine Vandaele[2]

[1]Instituto de Astrofísica de Andalucia, Granada, Spain
[2]Belgian Royal Institute for Space Aeronomy, Brussels, Belgium
[3]Graduate School of Frontier Sciences, The University of Tokyo
[4]NASA Goddard Space Flight Center, USA
[5]American University, Washington DC, USA
[6]Moscow Institute of Physics and Technology (MIPT), Moscow, Russia
[7]Space Research Institute (IKI), Moscow, Russia
[8]Karlsruhe Institute of Technology, Institute of Meteorology and Climate Research, Karlsruhe, Germany
[9]Space Science Institute, Boulder, USA
[10]Institute for Space Astrophysics and Planetology, Italy
[11]Open University, Milton Keynes, UK
[12]Graduate School of Science, Tohoku University, Sendai, Japan
[13]Laboratoire de Météorologie Dynamique, IPSL, Paris, France

Key Points:

- Global map of CO profiles from NOMAD SO observations during the first year of TGO operations is presented for the first time.
- During the onset of the 2018 global dust storm, the CO VMRs are found to be depleted by 28% at 50 km compared to the average CO VMR values.
- High CO abundance at tropospheric altitudes is observed over NH during decay of the global dust storm when the atmospheric dust loading is high.

Corresponding author: Ashimananda Modak, ashim@iaa.es

This article has been accepted for publication and undergone full peer review but has not been through the copyediting, typesetting, pagination and proofreading process, which may lead to differences between this version and the Version of Record. Please cite this article as doi: 10.1029/2022JE007282.

This article is protected by copyright. All rights reserved.

Accepted Article

21699100, ja, Downloaded from https://agupubs.onlinelibrary.wiley.com/doi/10.1029/2022JE007282 by The Open University, Wiley Online Library on [23/02/2023]. See the Terms and Conditions (https://onlinelibrary.wiley.com/terms-and-conditions) on Wiley Online Library for rules of use; OA articles are governed by the applicable Creative Commons License

Abstract

We present CO density profiles up to about 100 km in the Martian atmosphere obtained for the first time from retrievals of solar occultation measurements by the Nadir and Occultation for Mars Discovery (NOMAD) onboard ExoMars Trace Gas Orbiter (TGO). CO is an important trace gas on Mars, as it is controlled by CO_2 photolysis, chemical reaction with the OH radicals, and the global dynamics. However, the measurements of CO vertical profiles have been elusive until the arrival of TGO. We show how the NOMAD CO variations describe very well the Mars general circulation. We observe a depletion of CO in the upper troposphere and mesosphere during the peak period, L_S = 190°–200°, more pronounced over the northern latitudes, confirming a similar result recently reported by ACS onboard TGO. However, in the lower troposphere around 20 km, and at least at high latitudes of the S. hemisphere, NOMAD CO mixing ratios increase over 1500 ppmv during the GDS (Global Dust Storm) onset. This might be related to the downwelling branch of the Hadley circulation. A subsequent increase in tropospheric CO is observed during the decay phase of the GDS around $L_S = 210° - -250°$ when the dust loading is still high. This could be associated with a reduction in the amount of OH radicals in the lower atmosphere due to lack of solar insolation. Once the GDS is over, CO steadily decreases globally during the southern summer season. A couple of distinct CO patterns associated with the Summer solstice and equinox circulation are reported and discussed.

Plain Language Summary

CO is an extremely interesting trace species in the Martian atmosphere. It has been used for both dynamical and photochemical studies of the atmosphere. But its vertical distribution has not been systematically measured until the arrival of the Exomars Trace Gas Orbiter(TGO). We use observations of the NOMAD (Nadir and Occultation for Mars Discovery) spectrometer onboard TGO to retrieve full profiles of mixing ratios of CO up to 100 km with a good vertical resolution. The retrievals cover two Martian seasons during which a global dust storm event occurred. We have found the behavior of CO during this event to be governed by local chemistry as well as by the long range transport. During the dust storm, CO mixing ratios are depleted all over the globe while over the southern high latitudes we discover an increase in CO due to transport from low latitudes during the end of the southern winter. The dynamical effect of global transport

This article is protected by copyright. All rights reserved.

Accepted Article

21699100, ja, Downloaded from https://agupubs.onlinelibrary.wiley.com/doi/10.1029/2022JE007282 by The Open University, Wiley Online Library on [23/02/2023]. See the Terms and Conditions (https://onlinelibrary.wiley.com/terms-and-conditions) on Wiley Online Library for rules of use; OA articles are governed by the applicable Creative Commons License

is found in the vertical distribution of CO during the southern summer. Another important result, where the local chemistry might be at play is the increase of CO in the low altitudes over low and mid latitudes during the decay phase of the GDS.

1 Introduction

CO is a trace gas of large interest in the Martian atmosphere as its distribution is ruled by photochemistry and dynamics. It is produced in the upper atmosphere of Mars by photolysis of CO_2 and destroyed in the lower atmosphere by the hydroxyl radicals (OH) (McElroy & Donahue, 1972; Parkinson & Hunten, 1972). Due to the long photochemical lifetime of CO in the Martian atmosphere (González-Galindo et al., 2005) it can be used as a dynamical tracer. As a non-condensable gas, CO shows strong variations in the polar regions during sublimation and condensation of the polar caps and a slow seasonal variation in the low latitude region (Forget et al., 2008). The CO density can also be used to constrain dynamical parameters of models such as eddy diffusion coefficients in the homosphere (Rodrigo et al., 1990; Yoshida et al., 2022).

CO on Mars was first detected from Earth by Kaplan et al. (1969) using high resolution infrared Fourier spectroscopy. Later, ground based observations used infrared (Billebaud et al., 1991), microwave (Kakar et al., 1977; R. Clancy et al., 1983), millimeter (Lellouch et al., 1991), and submillimeter (Encrenaz et al., 1991) spectroscopy. In more recent ground based efforts, a positive north-to-south gradient of CO column averaged mixing ratio was found in latitudinal mapping during summer (Krasnopolsky, 2015) and an opposite trend was found during winter (Krasnopolsky, 2003). These ground based observations showed an average CO volume mixing ratio (VMR) around 800 ppmv, with significant seasonal and latitudinal variability.

Other instruments dedicated to the study of CO in the Mars' atmosphere are PFS (Planetary Fourier Spectroscopy) and OMEGA (Observatoire pour la Minéralogie, l'Eau, les Glaces et l'Activité) onboard MEX (Mars EXpress) (Encrenaz et al., 2006), CRISM (Compact reconnaissance imaging spectrometer for Mars) onboard MRO (Smith et al., 2009), and LNO (Limb Nadir Occultation) of NOMAD (The Nadir and Occultation for MArs Discovery instrument) onboard TGO (Trace Gas Orbiter) (Smith et al., 2021). All these instruments have significant coverage in both latitudes and seasons and have been operating for several years. Recently, PFS measurements for 7 Martian years were used

This article is protected by copyright. All rights reserved.

Accepted Article

21699100, ja, Downloaded from https://agupubs.onlinelibrary.wiley.com/doi/10.1029/2022JE007282 by The Open University, Wiley Online Library on [23/02/2023]. See the Terms and Conditions (https://onlinelibrary.wiley.com/terms-and-conditions) on Wiley Online Library for rules of use; OA articles are governed by the applicable Creative Commons License

to study the seasonality of CO from the nadir observations (Bouche et al., 2021). Another significant result found from the PFS observations is the low values of CO VMR (Sindoni et al., 2011) during the perihelion season from high southern latitudes to 50°N. In another study from the PFS observations, high constant values (1200 ppm) of the CO column is found during $L_S = 330°$-$360°$ (Billebaud et al., 2009). OMEGA measurements reveal the seasonal behavior of CO over the Hellas basin (Encrenaz et al., 2006) where CO mixing ratios increase by a factor of 2 during winter. These results from PFS and OMEGA indicate the seasonal and topographical effect on column abundance of CO. A more detailed study of CO column with seasonal and spatial variations was performed with the measurements from CRISM (Smith et al., 2009). These studies confirm depletion of CO due to the sublimation of polar ice, a behavior predicted by Ar distribution observed by the Gamma Ray Spectrometer (GRS) onboard Mars Odyssey spacecraft (Sprague et al., 2004) and the Mars Global Climate Model developed at the Laboratoire de Météorologie Dynamique (LMD-MGCM) (Forget et al., 2008) which is now known as Mars Planetary Climate Model (Mars PCM) (Forget et al., 2022). CRISM measurements also show a weak correlation of CO with surface pressure in the low latitude region (Smith et al., 2018).

From the above mentioned ground-based and space borne measurements, we know a great deal about the variation of the column averaged CO and its qualitative relation with the seasonal pressure cycle. Very recently, column averaged mixing ratio of CO is reported by Smith et al. (2021) from the LNO measurement of NOMAD. They have established a global average of 800 ppm. This revealed that CO seasonal variation is greater in the polar regions than at the equator. The column measurements are mostly representative of the surface CO VMR. However, in order to characterize its dynamical and chemical sources and sinks, and underlying atmospheric variability, the density measurements are necessary. For example, a recent study of the variation of Martian CO obtained from the MIR (mid-infrared) channel of ACS (Atmospheric Chemistry Suite) onboard TGO, found that CO is depleted during the MY 34 global dust storm (GDS) (Olsen et al., 2021). The seasonal coverage used in Olsen et al. (2021) was limited. An extended set of measurements from ACS but with a different spectral channel (NIR, near-infrared) is included in this special issue (A. Fedorova et al. (2022)) which includes comparisons with the measurements of MIR and TIRVIM.

Until the arrival of TGO, the empirical description of Martian CO density profiles, with a good resolution in the vertical and in a systematic manner, was essentially ab-

This article is protected by copyright. All rights reserved.

Accepted Article

21699100, ja, Downloaded from https://agupubs.onlinelibrary.wiley.com/doi/10.1029/2022JE007282 by The Open University, Wiley Online Library on [23/02/2023]. See the Terms and Conditions (https://onlinelibrary.wiley.com/terms-and-conditions) on Wiley Online Library for rules of use; OA articles are governed by the applicable Creative Commons License

sent. Here, we present vertical profiles of CO retrieved from the measurements recorded by NOMAD solar occultation (SO) for the first year of TGO observations from April 2018 to March 2019 , for the first time. This covers the last two seasons of MY 34 with fine latitudinal coverage. The characteristics of the chosen dataset corresponding to these observations are described in section 2 along with a brief description of the NOMAD SO channel. Section 3 is dedicated to the preparation or cleaning steps of the data analysis before they are used by our retrieval scheme. The retrieval scheme is described in detail with an example of a scan retrieval in section 4. Results of the CO retrieval from the above mentioned dataset are presented in section 5, where we describe the seasonal, latitudinal, and diurnal variation in the CO distribution. The next section also includes a proper comparison of the results with the model predictions.

2 The NOMAD Instrument and Dataset

NOMAD is a suite of three spectrometers onboard ExoMars Trace Gas Orbiter. Two spectrometers operate in the infra-red (IR), the SO and the LNO. A third spectrometer, UVIS (The Ultraviolet and Visible Spectrometer), operates in the ultraviolet and visible (Vandaele et al., 2018, 2015). SO performs solar occultation and LNO performs both limb scanning and nadir observation. The UV spectrometer is capable of scanning the Mars atmosphere both in solar occultation and nadir viewing mode (Patel et al., 2017). In this work, we will analyze data from the SO channel. This channel covers a spectral range $2.2 - 4.3$ μm and it has a nominal resolving power of $20,000$ (Neefs et al., 2015). NOMAD SO uses an echelle grating in Littrow configuration which means the incident, reflected and Blaze angles are equal for this configuration (Neefs et al., 2015). The other components of the SO channels are the detector, parabolic mirrors, and Acousto Optical Tunable Filter (AOTF). The NOMAD SO detector has 320 columns for the spectral dimension and 256 for the spatial dimension. The AOTF acts as a bandpass filter controlled by radio frequency input. Ideally, it selects one wavelength range for a radio frequency input and sends it to the grating through parabolic mirrors, and diffracted light falls on the detector after being guided by the parabolic mirrors. The wavenumber range limit of the AOTF is adjusted to ideally capture only one diffraction order at a time. In practice, adjacent diffraction orders do overlap and in the case of NOMAD SO see section 3, this adds non-negligible components which need to be taken into account in the forward model (Liuzzi et al., 2019; Villanueva et al., 2022). A quantitative description

This article is protected by copyright. All rights reserved.

Accepted Article

21699100, ja, Downloaded from https://agupubs.onlinelibrary.wiley.com/doi/10.1029/2022JE007282 by The Open University, Wiley Online Library on [23/02/2023]. See the Terms and Conditions (https://onlinelibrary.wiley.com/terms-and-conditions) on Wiley Online Library for rules of use; OA articles are governed by the applicable Creative Commons License

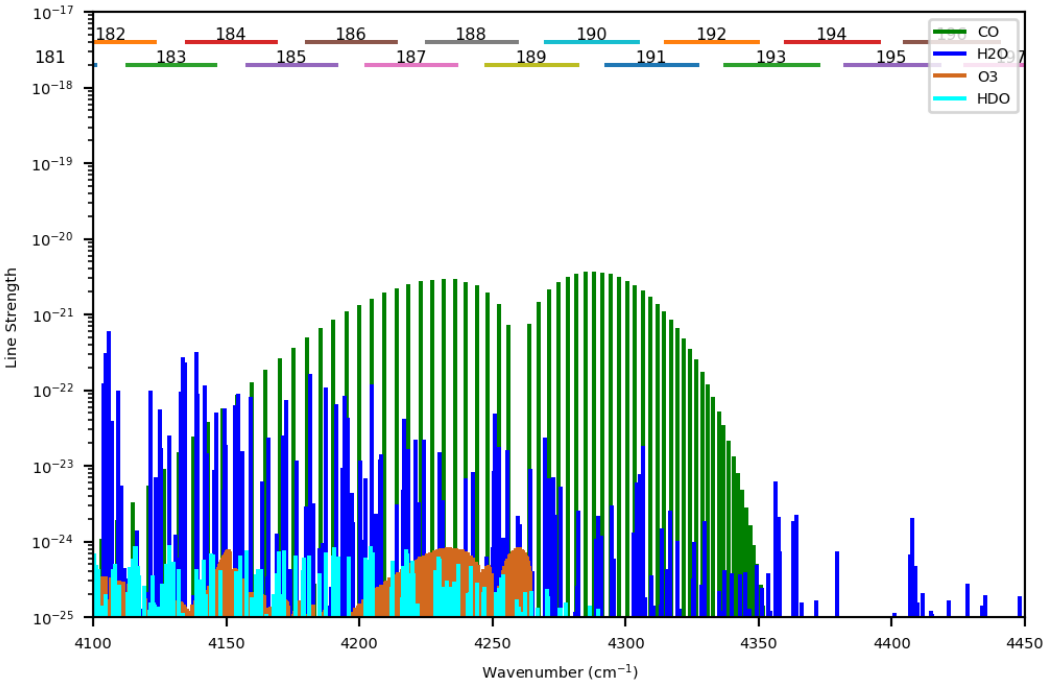

Figure 1. Spectral location of NOMAD SO diffraction orders for CO, and other atmospheric species with indication of strength of the strongest ro-vibrational absorption lines. The positions and line strengths are from HITRAN 2016 (Gordon et al., 2017).

of this contamination for the CO orders used in this work is presented below in section 3. Once the diffraction order is selected, the incoming radiation is dispersed through the grating and incident on the detector's pixels. The intensity distribution of the diffraction order depends on the AOTF transfer function and the blaze function (Liuzzi et al., 2019). The blaze function characterizes the diffraction efficiency of grating depending on the wavelength. These two functions, i.e., the AOTF transfer function and the grating blaze function need to be very well characterized in order to simulate the NOMAD measured radiance correctly. For the complete optical description of the SO channel, one can refer to Neefs et al. (2015).

The NOMAD diffraction orders suitable for CO retrievals are shown in Figure 1, together with line positions from HITRAN 2016 (Gordon et al., 2017). In the NOMAD SO spectra, the CO rotational-vibrational lines are well separated and there is no significant absorption from other atmospheric species such as H_2O, CO_2 in the orders between 186 and 191. The H_2O lines are shown for comparison purposes only; they are much weaker than the CO lines and are not observed in the NOMAD data. We choose order

This article is protected by copyright. All rights reserved.

Accepted Article

21699100, ja, Downloaded from https://agupubs.onlinelibrary.wiley.com/doi/10.1029/2022JE007282 by The Open University, Wiley Online Library on [23/02/2023]. See the Terms and Conditions (https://onlinelibrary.wiley.com/terms-and-conditions) on Wiley Online Library for rules of use; OA articles are governed by the applicable Creative Commons License

190 for the retrieval because some of the strongest CO absorption lines lie in this order. Also, the number of atmospheric scans performed by NOMAD SO is much larger than in any other diffraction order during the first year of operations.

3 Data Cleaning and Pre-processing

In this work, we use NOMAD Level 1 calibrated transmittances. These are downloaded as formatted data and provide values of atmospheric transmittances, measurement noise, and calibration parameters such as the parameters for the pixel to wavenumber conversion, the center of the blaze function, etc. We first clean these transmittances from diverse systematics such as spectral bending and shift (see section 3.2). before ingesting it into the actual inversion scheme. We call this internal step pre-processing and it is described below in section 3.2. Both pre-processing and retrieval, make use of a line-by-line forward model, central to our analysis, which is described next.

3.1 The KOPRA Forward Model

We use the Karlsruhe Optimized and Precise Radiative transfer Algorithm (KOPRA) described in Stiller (2000), to simulate the NOMAD SO measurements, both during the "data cleaning" phase and at the core of the inversion processor. KOPRA has been widely used for the retrievals of Earth atmospheric gases and aerosols (Schreier et al., 2018; Höpfner & Emde, 2005). KOPRA solves the radiative transfer (RT) equation in a line-by-line approach to calculate monochromatic radiance. In our adaptation to Mars solar occultation conditions, the atmosphere is divided into layers of 1 km width from the ground to 60 km, layers of 2 km from 60 km to 90 km, 2.5 km from 90 km to 130 km, and 5 km from 130 km to 220 km. The RT calculations are done along the line of sight of the observations. The model calculates the line absorptions from the spectroscopic information provided by the HITRAN 2016 database (Gordon et al., 2017).

The instrumental line shape (ILS) of the NOMAD SO is one of the essential parameter for atmospheric retrievals as it reflects the manner in which the spectra are recorded across the detector (Liuzzi et al., 2019; Aoki et al., 2021; I. R. Thomas et al., 2022). The NOMAD SO instrumental response, including the AOTF and the ILS have been the subject of a recent revision, and we use a parameterization from a consolidated approach in collaboration with various teams within the NOMAD consortium (Villanueva et al.,

This article is protected by copyright. All rights reserved.

Accepted Article

21699100, ja, Downloaded from https://agupubs.onlinelibrary.wiley.com/doi/10.1029/2022JE007282 by The Open University, Wiley Online Library on [23/02/2023]. See the Terms and Conditions (https://onlinelibrary.wiley.com/terms-and-conditions) on Wiley Online Library for rules of use; OA articles are governed by the applicable Creative Commons License

2022). The ILS is parameterized as double Gaussian function. Its peaks, widths and the distance between the Gaussian functions for every order have been determined combining several analytical and retrieval methods. The variability of the ILS within each order and across orders is a NOMAD-SO specific difficulty which we consider as well characterized, as can be seen from inspection of the retrieval's residuals. However, for the AOTF transfer function, its parameterization is further fine-tuned around the values suggested by Villanueva et al. (2022). This fine-tuning is described in Appendix A, and permitted a significant improvement in the retrievals. We convolved the KOPRA spectra with the revised ILS, the fine-tuned AOTF, and the blaze function (Brines et al., 2022). This convolution is done within the forward model.

3.2 Pre-processing

An example of NOMAD calibrated transmission data from one particular scan in diffraction order 190 is shown in Figure 2, panel a. Recorded against pixel number, transmittances are transformed into wavenumber dependent function during the nominal calibration, using a second order polynomial relation between wavenumber and pixel number (Liuzzi et al., 2019). The different colors correspond to different tangent heights, and the vertical lines in red indicate the position of the center of the CO rotational-vibrational lines for the main order 190. The transmittances clearly suffer from spectral shift and bending of the continuum across the detector (Figure 2, panel a) which occurs due to thermally induced mechanical stress on the detector Liuzzi et al. (2019). This bending effect is almost ubiquitus, present in all NOMAD orders at all altitudes and scans (Vandaele et al., 2018). It changes from each altitude to the next in a quasi-random manner, and systematically responds to a (variable) 4th order polynomial. Notice that this is very different to the atmospheric continuum due to aerosols absorption, which can be considered as spectrally constant due to the narrow span of the NOMAD orders (Vandaele et al., 2018) and which is usually important at low altitudes.

Before using these data in a proper inversion of densities they need to be corrected for these two effects. For this purpose, the NOMAD transmittances are divided into small micro-windows (MW) containing at least one absorption line (see Figure 2). The spans of these MWs are shown in Figure 2 and are 4273.50 - 4275.80 cm^{-1}, 4277.20 - 4282.200 cm^{-1}, 4283.2 - 4288.80 cm^{-1}, 4290.00 - 4295.20 cm^{-1}, and, 4296.20 - 4301.00 cm^{-1}.

This article is protected by copyright. All rights reserved.

Accepted Article

21699100, ja, Downloaded from https://agupubs.onlinelibrary.wiley.com/doi/10.1029/2022JE007282 by The Open University, Wiley Online Library on [23/02/2023]. See the Terms and Conditions (https://onlinelibrary.wiley.com/terms-and-conditions) on Wiley Online Library for rules of use; OA articles are governed by the applicable Creative Commons License

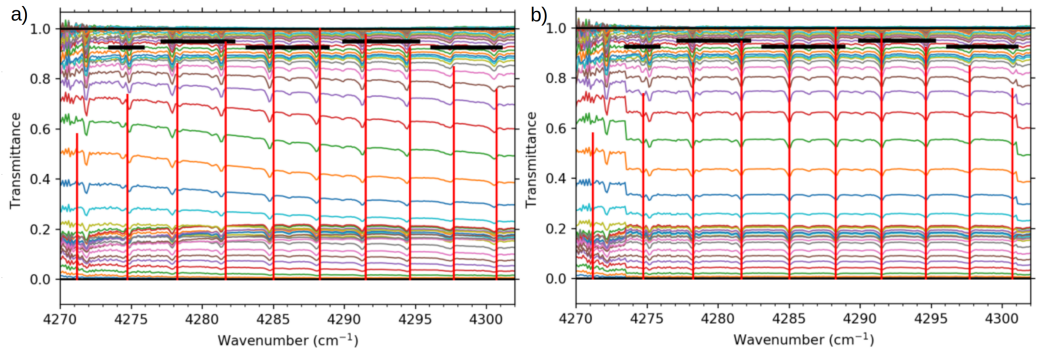

Figure 2. Example of our cleaning method applied to diffraction order 190 in one specific scan (20180503_151030_SO_A_E). Panel a, all the original spectra (calibrated transmittances) taken in this scan, showing clear bending effects and spectral shifts. Panel b, spectra after cleaning. Notice the cleaning is only applied to a subset of the full diffraction order. Vertical red solid lines indicate the expected position of the CO spectral lines (HITRAN 2016). The five short horizontal lines in black near the top of the panels indicate the microwindows used for this cleaning. see text for details.

Starting with the bending effect, in all NOMAD orders this is usually very small in the central part of the order. In each order it is corrected using a polynomial fitting to the background continuum or baseline, as simulated with KOPRA at each tangent altitude. This correction is used as a multiplicative factor because the ultimate reason for this effect comes from small changes in the AOTF response during each SO scan. This explains the spectrally low variation (4th polynomial) in the spectra. During these changes the AOTF varies very little in the center of the order, where it is essentially one. Therefore the effect on the measured radiances should be multiplicative, and consequently, also on the transmittances. The use of a line-by-line calculation at each altitude to correct for the bending guarantees that the effect from gas line-overlapping is taken into account and is separated from the actual bending effect. Still, this correction may be a source of uncertainty for the retrieval of aerosol properties, and a simple strategy to minimize this is to select the center of the order to derive them at each altitude. This is the topic of another work (Stolzenbach et al., 2022) by our team, also submitted to this special issue.

Regarding the spectral shift, present in all spectra, i.e., at all altitudes, and variable from scan to scan, this is determined from comparisons of data and model simu-

This article is protected by copyright. All rights reserved.

Accepted Article

21699100, ja, Downloaded from https://agupubs.onlinelibrary.wiley.com/doi/10.1029/2022JE007282 by The Open University, Wiley Online Library on [23/02/2023]. See the Terms and Conditions (https://onlinelibrary.wiley.com/terms-and-conditions) on Wiley Online Library for rules of use; OA articles are governed by the applicable Creative Commons License

lations at all altitudes with significant line absorption (to minimize errors during its determination). These spectral shifts, as it also occurs in other diffraction orders, vary across the order in a linear manner. A linear function is fitted on the values of the shifts obtained for each MW, and this is interpolated across the wavenumber range of the spectra for a full-order correction. Microwindows near the edge of the order are not considered due to higher noise there. Details of these corrections are presented in a companion paper in this special issue (López Valverde et al., 2022).

Our inversion scheme uses radiances instead of transmittances. Thus the cleaned Level-1a transmittances are converted into solar radiances using a space view simulation with KOPRA, at 220 km tangent altitude, using the AOTF appropriate for this diffraction order and the grating properties described by the blaze function (Liuzzi et al., 2019). The space view radiance is calculated using a reference solar radiance supplied externally. This reference radiance has no other function and has no impact on the inversion.

One additional caution, related to the MWs selection, deserves some discussion. As mentioned before, one characteristic of real AOTF spectrometers is that the addition of adjacent diffraction orders to the main order is not negligible. These contributions, when added to the forward model, guided the selection of the MWs in this study (Villanueva et al. (2022) also see Appendix A). Figure 3 shows one example of this contamination by adjacent orders in the case of order 190. The vertical lines in the plot indicate the positions of CO absorption lines from different adjacent orders. The main order is indicated with the solid green color and the adjacent orders on both sides with the same color but with a solid line on the left and with a dotted line on the right. Three central absorption lines of the spectra within $4285\,\mathrm{cm}^{-1}$ and $4292\,\mathrm{cm}^{-1}$ are not at all contaminated with the absorption from the adjacent orders. As can be seen from Figure 3 most of the contaminations are from orders 187, 188, 189 on the left and 191 on the right. A maximum of four orders contamination to either sides is shown in Figure 3 which is sufficient to explain the absorption line in the diffraction order 190. This contamination, in addition to line strength considerations, was taken into account during the selection of the MWs used in this work. For the inversion of CO (next section) we finally selected two MWs near the center of the order, shown in Figure 3.

This article is protected by copyright. All rights reserved.

Accepted Article

21699100, ja, Downloaded from https://agupubs.onlinelibrary.wiley.com/doi/10.1029/2022JE007282 by The Open University, Wiley Online Library on [23/02/2023]. See the Terms and Conditions (https://onlinelibrary.wiley.com/terms-and-conditions) on Wiley Online Library for rules of use; OA articles are governed by the applicable Creative Commons License

Accepted Article

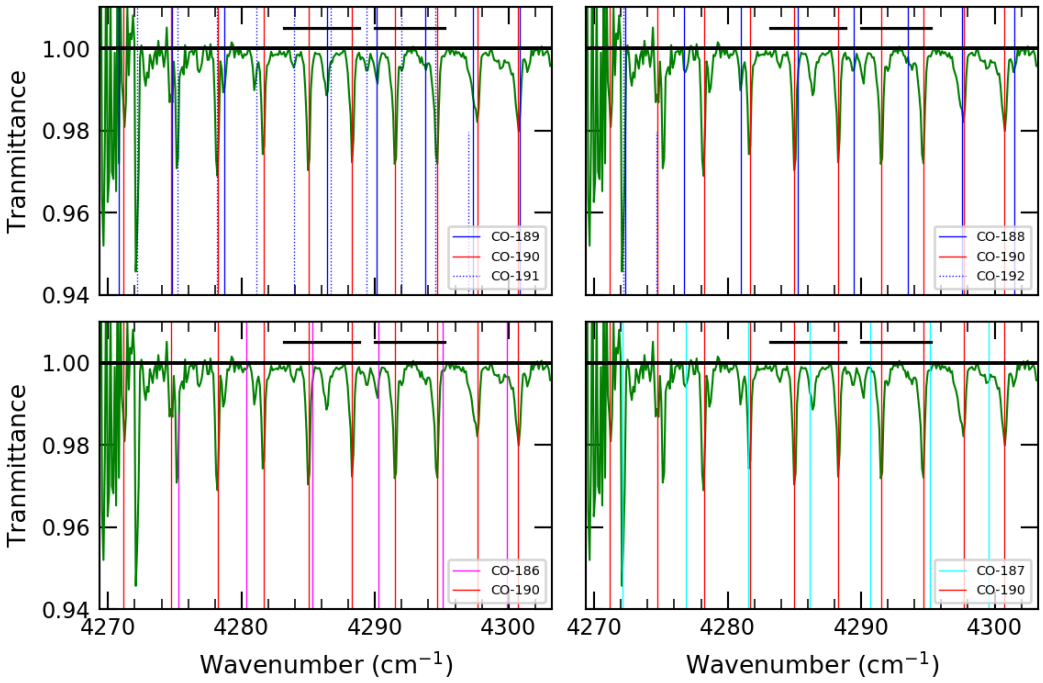

Figure 3. Example of contamination from the four adjacent orders at each side of the principal diffraction order 190. Colored vertical lines represent the position of the CO absorption present in the different orders as indicated in the legends. Four panels are used for clarity, showing different adjacent orders in each of them versus the central order 190. The selected MWs for the inversion are shown in thick black horizontal lines. See text for details.

This article is protected by copyright. All rights reserved.

21699100, ja, Downloaded from https://agupubs.onlinelibrary.wiley.com/doi/10.1029/2022JE007282 by The Open University, Wiley Online Library on [23/02/2023]. See the Terms and Conditions (https://onlinelibrary.wiley.com/terms-and-conditions) on Wiley Online Library for rules of use; OA articles are governed by the applicable Creative Commons License

4 Retrieval Scheme

After the cleaning of the Level-1a transmission data described above, we performed the CO retrieval using an inversion processor called Retrieval Control Programming (RCP) described in von Clarmann et al. (2003). We summarize here some of its characteristics. Our global-fit retrieval scheme and application are common to other NOMAD retrieval targets at the IAA team, including H_2O (Brines et al., 2022), temperature and CO_2 densities (Lopez-Valverde et al, 2022), and aerosols (Stolzenbach et al., 2022), all in this special issue.

RCP uses KOPRA as its forward model and follows a usual iterative approach to solve the inverse solution to the RT equation, based upon a Levenberg-Marquardt least square minimization algorithm. RCP can use diverse solution methods, like an optimal estimation approach, but in this work, we use a more flexible first order Tikhonov regularization. In each iteration, it runs KOPRA and the simulated spectra are compared to the measured ones at each altitude simultaneously until convergence is reached when the variation in the target quantities are smaller than a fraction of the noise error (Jurado Navarro et al., 2016). RCP also provides averaging kernel (AK) and noise error for the target. The AK is expressed as $\boldsymbol{A} = \boldsymbol{GK}$ where $\boldsymbol{G}$ is the gain matrix and $\boldsymbol{K}$ is Jacobian matrix (Rodgers, 2000). The gain matrix is defined in Rodgers (2000) as follows,

$$\boldsymbol{G} = (\boldsymbol{K}^T \boldsymbol{S}^{-1} \boldsymbol{K} + \boldsymbol{R})^{-1} \boldsymbol{K}^T \boldsymbol{S}_y^{-1}. \tag{1}$$

$\boldsymbol{K}$ is the Jacobian matrix, $\boldsymbol{S}_y$ is the covariance matrix for the measurement noise and $\boldsymbol{R}$ is the regularization matrix. The value of the AK is always below unity. The noise error is mapped onto the retrieval grid as defined in the equation below.

$$\boldsymbol{S}_x = \boldsymbol{G}^T \boldsymbol{S}_y \boldsymbol{G}. \tag{2}$$

The $\boldsymbol{\chi^2}$ is defined as:

$$\boldsymbol{\chi^2} = (\boldsymbol{y} - \boldsymbol{F(x)})^T \boldsymbol{S}_y^{-1} (\boldsymbol{y} - \boldsymbol{F(x)}) + (\boldsymbol{x} - \boldsymbol{x}_a)^T \boldsymbol{R} (\boldsymbol{x} - \boldsymbol{a}), \tag{3}$$

where $\boldsymbol{y}$ is the measurement, $\boldsymbol{F}(\boldsymbol{x})$ is the forward model $\boldsymbol{x_a}$ is the *a priori* state vector and $\boldsymbol{x}$ is the true state vector which includes our target CO abundance profile. The retrieval of CO with our retrieval scheme is found to be robust against large variations in the *a priori* values of CO (see Appendix B).

This article is protected by copyright. All rights reserved.

Accepted Article

21699100, ja, Downloaded from https://agupubs.onlinelibrary.wiley.com/doi/10.1029/2022JE007282 by The Open University, Wiley Online Library on [23/02/2023]. See the Terms and Conditions (https://onlinelibrary.wiley.com/terms-and-conditions) on Wiley Online Library for rules of use; OA articles are governed by the applicable Creative Commons License

The *a priori* CO profiles extended from the planet's surface up to 200 km and are obtained from the Mars PCM (Forget et al., 1999; Lefèvre et al., 2021) using the dust scenarios for MY 34 and MY 35 (Montabone et al., 2015, 2020). The model uses dust and water cycles described in (Navarro et al., 2014). The model outputs are at defined grids and are interpolated to the time and location of the NOMAD SO observation. The atmosphere needed by the forward model is built using the pressure and temperature retrieved from SO observation of diffraction order 149 (López Valverde et al., 2022).

In a typical CO VMR profile retrieval, RCP performs the simultaneous inversion of 3 quantities or targets, the CO VMR, a spectral shift, and a baseline accommodating factor named scale-h. The shift is used as a target with the intention to detect any residual spectral shift remaining after the correction already performed at the pre-processing level. Scale-h is a spectrally constant transmittance level within each MW, adjusted to account for the impact of aerosol absorption on the continuum and any small remaining calibration biases in each MW. As mentioned above, the continuum absorption within the narrow NOMAD diffraction orders is spectrally flat (Vandaele et al., 2018) but with this Scale-h parameter we allow for small variations between MWs.

Before the actual application to real measurements, an extensive study of synthetic retrievals, generated using KOPRA, was performed. These were very useful to test the performance of the inversion, its independence on *a priori* assumptions, and to fine-tune the regularization. Appendix B presents some details and results from the synthetic retrievals.

4.1 Typical Retrieval Performance

To illustrate the performance of an inversion scheme, it is of paramount importance to examine the residuals or best fit obtained, and to characterize the error propagation and vertical resolution by an analysis of the AKs.

An example of the best fit spectrum achieved with our inversion scheme is shown in the upper panel of Figure 4, for one particular scan and a tangent altitude of 74 km. Figure 4 also shows the spectrum generated with the *a priori* CO profile, for comparison. The lower panel depicts the residual transmittances (at the end of the iteration and convergence) together with the model-data difference when using the *a priori*. The best

This article is protected by copyright. All rights reserved.

Accepted Article

21699100, ja, Downloaded from https://agupubs.onlinelibrary.wiley.com/doi/10.1029/2022JE007282 by The Open University, Wiley Online Library on [23/02/2023]. See the Terms and Conditions (https://onlinelibrary.wiley.com/terms-and-conditions) on Wiley Online Library for rules of use; OA articles are governed by the applicable Creative Commons License

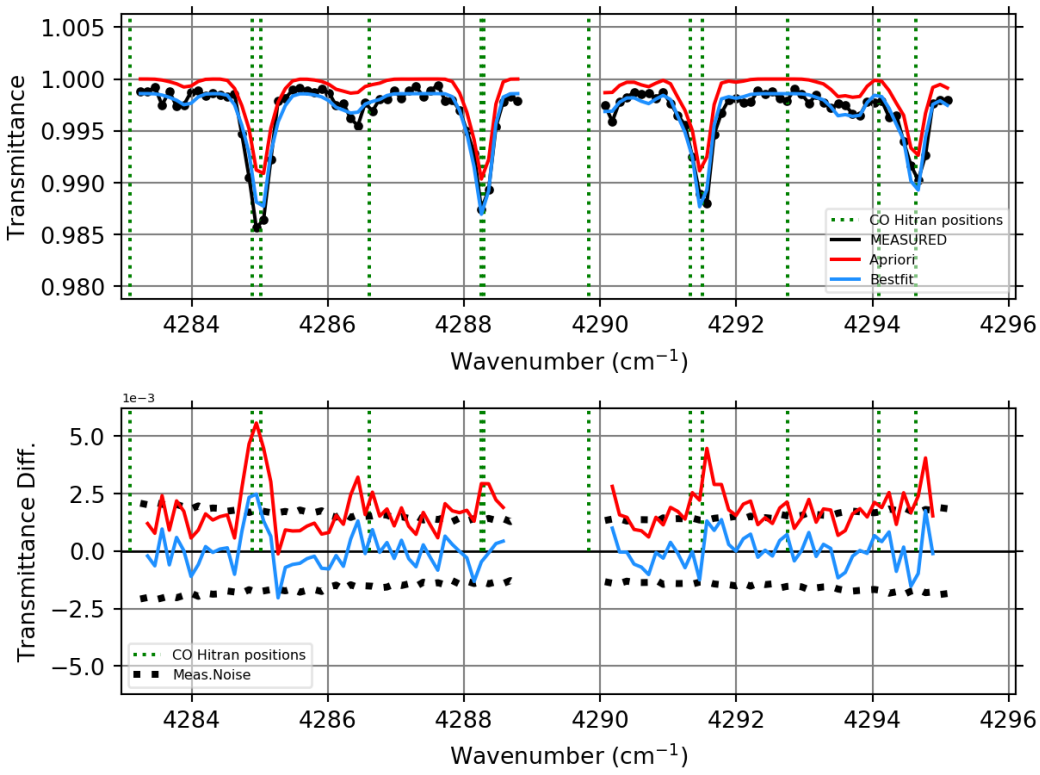

Figure 4. Best fit spectrum to the NOMAD cleaned transmittances at a tangent altitude of about 74 km from scan 20180801 055956 SO A E 190 (Lat 66°N, Lon 161°W, Ls 222°). The top panel shows the measured spectrum in solid black line with dots, the best fit spectrum at the end of the inversion is blue, and the spectrum obtained with the *a priori* atmospheric profile in red. The spectrum is split in 2 segments which correspond to the 2 MWs used in the inversion. The lower panel shows the residuals (Model fit - NOMAD) in blue, together with the same quantity but calculated with the model spectrum for the *a priori* atmosphere, in red. The dotted lines represent the NOMAD SO measurement errors used in the inversion.

fit residual transmittance spectrum lies within the limit of the measurement noise at all wavenumbers.

Figure 5 shows a set of typical diagnostics for the scan in Figure 4. From left to right, the four panels show the retrieved CO profile, the rows of the AK, the percentage error at each altitude, and the vertical resolution profile, respectively. The averaging kernel shows the mapping of the measurements onto the retrieval grid. The vertical resolution is the usual interpretation of the full width at half maximum of the AK at each retrieval altitude. The CO VMRs retrieved in this example are greater than the

This article is protected by copyright. All rights reserved.

Accepted Article

21699100, ja, Downloaded from https://agupubs.onlinelibrary.wiley.com/doi/10.1029/2022JE007282 by The Open University, Wiley Online Library on [23/02/2023]. See the Terms and Conditions (https://onlinelibrary.wiley.com/terms-and-conditions) on Wiley Online Library for rules of use; OA articles are governed by the applicable Creative Commons License

a priori (shown in red), specially above 60 km. The errors are typically within 10%−15% below 80 km. The vertical resolution is within 5 km in the region below 80 km and increases with altitude, as the measurement noise and the retrieval error also do. The shaded region below 28 km, in the first panel, indicates the altitude where the slant optical depth is larger than 1.5. We do not retrieve CO in the altitudes with high dust opacities to avoid biases from the severe contamination in (reduction of) the spectral absorption lines. For such spectra, the averaging kernel values obtained in the retrieval diagnostics are zero, corresponding to no information.

After few experiments, we make use of a minimum value (0.03) of the AK. Retrieved CO densities with AKs below this minimum are not trusted. All the results presented in this study are qualified by this condition. Figure 5, panel b shows the diagonal of the AKs for a typical NOMAD SO scan and we observe that below about 80 km and down to 60 km these peaks are basically constant and they show small trend, with decreasing values below 60 km. This slow decrease in the AK could be indicative of line saturation. The lines used in order 190 are among the strongest in the IR spectrum. We made a study of the line depths in these limb geometry data in a small number of solar occultation scans. This study show us that the saturation effect in the line absorption start below about 80 km and becomes stronger. However, our forward model is a state-of-the-art line-by-line radiative transfer code that reproduces well the saturation effects in the line absorption. In the case of saturated absorption lines, the information is mostly derived from the wings of the absorption lines, because the line depth at the line centre does not vary with the increasing CO density. How much information can be extracted, i.e., how large is the sensitivity to the CO density, is provided by the AKs.

4.2 Effect of Climatology on Retrieved CO

We studied the effect of the *a priori* temperature, by using the PCM as a reference and adding ad-hoc perturbations on this profile. Here we discuss one example, for scan 20180423 204351 1p0a SO A I 190. Figure 6, shows two retrievals, from the same SO scan using two sets of pressures and temperatures. The profiles in black correspond the *a priori* obtained from the PCM. The red lines correspond to the retrieval using as *a priori* the T/P profile obtained from the inversion of this NOMAD SO scan (in diffraction order 149, results obtained by López Valverde et al. (2022). The retrieved CO VMR and absolute number densities in the two cases are shown in panels c and d respectively.

This article is protected by copyright. All rights reserved.

Accepted Article

21699100, ja, Downloaded from https://agupubs.onlinelibrary.wiley.com/doi/10.1029/2022JE007282 by The Open University, Wiley Online Library on [23/02/2023]. See the Terms and Conditions (https://onlinelibrary.wiley.com/terms-and-conditions) on Wiley Online Library for rules of use; OA articles are governed by the applicable Creative Commons License

Accepted Article

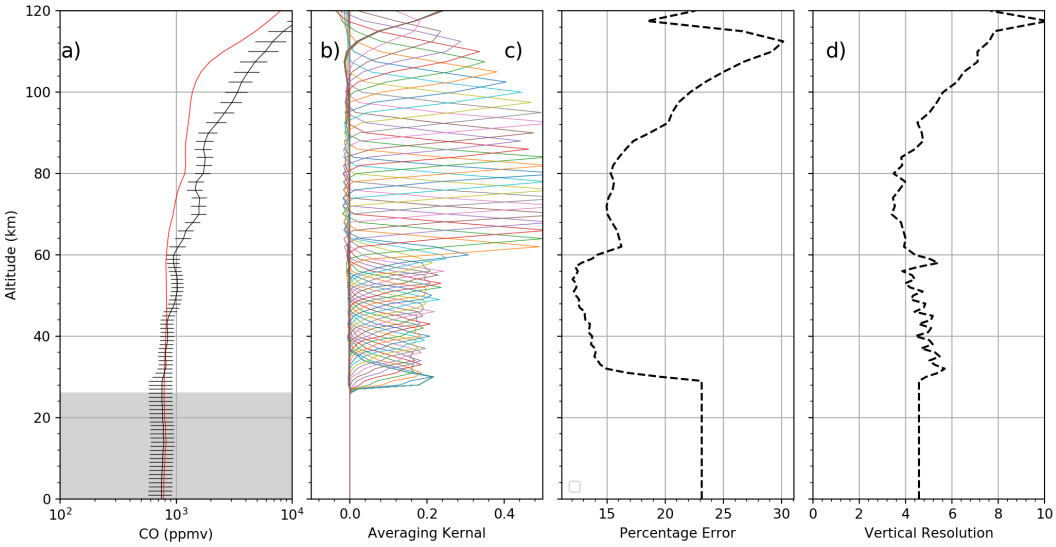

Figure 5. Retrieved CO profile from the same scan as in Figure 4 with error bars (panel a). The red line is the *a priori* profiles, the black line is the retrieved CO. The shaded area below 28 km represents the region of very high dust loading, where the SO spectra are not inverted. Panel b: selected rows of the Averaging Kernel matrix; the sharp change in the peak of the averaging kernel at 60 km is due to the change in the retrieval grid (see section 3.1 for the retrieval grid definition). Panel c: percentage error in the CO profile. Panel d: Vertical resolution, as given by the widths of the averaging kernel rows.

This article is protected by copyright. All rights reserved.

21699100, ja, Downloaded from https://agupubs.onlinelibrary.wiley.com/doi/10.1029/2022JE007282 by The Open University, Wiley Online Library on [23/02/2023]. See the Terms and Conditions (https://onlinelibrary.wiley.com/terms-and-conditions) on Wiley Online Library for rules of use; OA articles are governed by the applicable Creative Commons License

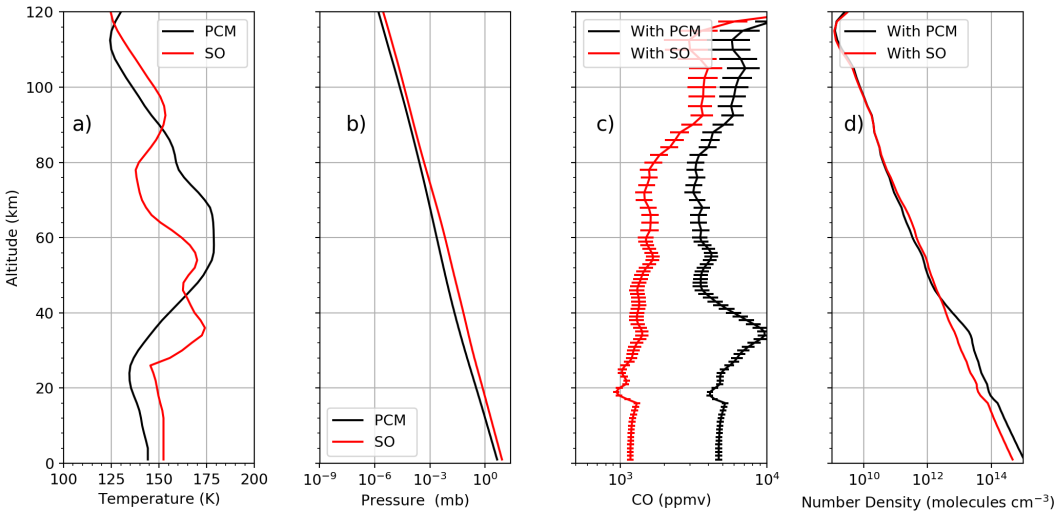

Figure 6. The effect of the reference thermal structure on the retrieved CO. Panel a: Temperature profiles from PCM (black line) and from NOMAD retrievals in order 149 (red line). Panel b: Pressure profiles from PCM (black) and from NOMAD (red). Panel c: retrieved CO VMR using the PCM inputs (black line) versus the NOMAD retrievals (red lines). Panel d: Same as Panel c but for the CO local number density (cm^{-3})

The obtained NOMAD pressures are higher than the PCM ones at each altitude, which in turn, results in a lower VMR than when using the PCM. The absolute CO density should be more independent of the densities assumed than the CO VMR, and this indeed observed above 50 km. But this is not the case of its dependence on the temperatures. And we observed in panel (d) that the CO absolute densities are varying with the assumed temperatures, with a crossing point around 45 km tangent height, which is present in both temperature and retrieved CO. Since this temperature effect is very important, in this work, we only used scans for which retrieved NOMAD temperatures are available (from a parallel effort in our team, see companion paper on temperature retrievals led by M. A. Lopez-Valverde in this special issue). In other words, we only considered the subset of NOMAD SO scans where orders 190 and 149 were measured simultaneously, and the final set consists of those where the temperature converged, which is a very high percentage of the available scans (López Valverde et al., 2022). This is done regardless of the difference between the *a priori* and the retrieved thermal structure.

This article is protected by copyright. All rights reserved.

Accepted Article

21699100, ja, Downloaded from https://agupubs.onlinelibrary.wiley.com/doi/10.1029/2022JE007282 by The Open University, Wiley Online Library on [23/02/2023]. See the Terms and Conditions (https://onlinelibrary.wiley.com/terms-and-conditions) on Wiley Online Library for rules of use; OA articles are governed by the applicable Creative Commons License

Accepted Article

5 Results and Discussion

The results of all our retrievals are shown in Figure 7. Due to the large variation in the CO relative abundance with altitude, we show the CO VMR values in log scale. The dataset extends from $L_S = 160°$ to $L_S = 354°$ (Figure 7, panels a and b) covering important seasons such as the onset of the global dust storm ($L_S = 190°$) (Guzewich et al., 2019), the GDS decay phase ($L_S > 235°$), the end of the southern spring ($L_S = 245°--263°$), and the whole of the southern summer. In this section, following López Valverde et al. (2022), we refer to the atmospheric region from the surface up to 50 km as troposphere, and to that above as mesosphere.

5.1 Seasonal Variation of CO

CO is a long lived gas species affected by the general circulation in the Martian atmosphere, and therefore an excellent tracer of the global dynamics on Mars (Lefèvre & Krasnopolsky, 2017). Figure 7 permits some insight into the seasonal variation of the CO VMR; panels c and d show the CO VMR distribution over the northern and southern hemispheres respectively. In general, and in agreement with PCM simulations, we observe a CO VMR increasing with altitude in the upper troposphere and through the mesosphere, as a result of the downward mixing from the CO source region at high altitude, following CO_2 photodissociation (Krasnopolsky, 1995; González-Galindo et al., 2009; Modak et al., 2020). Particularly large values and gradients are observed above about 60 km, but with significant variations. This variability can be better visualized by inspecting a given CO VMR iso-contour in Figure 7, like the value of 2500 ppmv (in orange color). This value is arbitrary but serves as a marker between two altitude regions with different physics regarding CO; the upper one driven by photochemical production and the lower one dominated by CO losses. CO VMR values as large as 2500 ppmv occur very high in the atmosphere at mid and low latitudes, following CO_2 photodissociation, but can be seen at much lower altitudes towards the poles due to global dynamics, as discussed below in section 5.2. This iso-contour is therefore particularly useful to illustrate the CO variability, both with season and latitude. Panels a and b show the track of the solar occultation, where this mix of changes with season and latitude can be seen. Latitude has a large impact, different in the north and south hemispheres since the coverage of high latitudes is different in each hemisphere. Over the southern high latitudes the occultation spent less time which produces sudden changes in the iso-contour. As

This article is protected by copyright. All rights reserved.

21699100, ja, Downloaded from https://agupubs.onlinelibrary.wiley.com/doi/10.1029/2022JE007282 by The Open University, Wiley Online Library on [23/02/2023]. See the Terms and Conditions (https://onlinelibrary.wiley.com/terms-and-conditions) on Wiley Online Library for rules of use; OA articles are governed by the applicable Creative Commons License

we discuss below in section 5.2, it is possible to decouple the latitudinal and seasonal trends to study only one of these, for example latitudinal variation for a small seasonal period.

There are two essential and different seasons where the dynamical behavior of the Martian atmosphere is distinct, the equinoxes and the solstices. So, we analyze here the CO distribution in these two periods, and also its variability in between. During the northern autumn equinox period ($L_S = 160° - -180°$) when two Hadley cells extend from the equator to high latitudes (Forget et al., 1999) and the solar insolation is similar in both hemispheres, we expect similar CO mixing ratios at similar latitudes in the north and south. And this is apparently the case in Figure 7, although unfortunately, only a few NOMAD scans are available during that period. For example, over the northern high latitudes ($> 60°$N) high values ($\sim$ 1500 ppm) of CO VMRs are observed down to 20 km. Similar values of CO are also observed over the southern latitude 60°S.

The appearance of the MY 34 GDS in 2018 perturbed the global circulation and we expect the CO distribution to depart from what should be its regular seasonal cycle. We observe in Figure 7 that during the onset of the GDS in the period $L_S = 190°$ to $L_S = 205°$, the high altitude VMRs decrease (when looking at a fixed altitude, specially in the mesosphere). This shows the well known tropospheric warming by solar heating of aerosols and the associated upwards expansion in atmospheric density, moving our iso-contour of 2500 ppm up to 100 km in the NH (northern hemisphere) during the GDS peak ($L_S = 205°$). Over the southern polar latitudes, however, the aerosols amount were lower, and that CO VMR iso-contour can be seen around 75 km.

After the onset of the GDS, the 2500 ppmv iso-contour shows a CO VMR quickly increasing at all mesospheric altitudes in the NH until $L_S \sim 225°$. During the GDS, the high dust loading warms (and expand) the atmosphere which, in turn, reinforces the hemispheric Hadley cells. This increased circulation, has been shown to transport trace gases up to mesopheric altitudes (Neary et al., 2020; Vandaele et al., 2019; Shaposhnikov et al., 2019; R. T. Clancy et al., 2010). Since $L_S \sim 225°$ until about $L_S \sim 282°$ the iso-contour stays approximately constant at 70 km tangent height. Surely the first part of this period is dominated by the decay phase of the GDS while the second may be more typical of a seasonal behavior, i.e., typical of a non-GDS year. The time evolution of the mesospheric CO VMR over SH (southern hemisphere) at mid-latitudes does not show those two different periods after the GDS. We observe a steadily small decrease with time

This article is protected by copyright. All rights reserved.

Accepted Article

21699100, ja, Downloaded from https://agupubs.onlinelibrary.wiley.com/doi/10.1029/2022JE007282 by The Open University, Wiley Online Library on [23/02/2023]. See the Terms and Conditions (https://onlinelibrary.wiley.com/terms-and-conditions) on Wiley Online Library for rules of use; OA articles are governed by the applicable Creative Commons License

up to about $L_S = 300°$. Our iso-contour is located at higher altitudes than in the NH, which shows an inter-hemispheric asymmetry, specially evident around the southern summer solstice, $L_S = 270°$. At the end of the southern summer, after $L_S = 330°$, the CO VMRs increase all over the globe, in both hemispheres. This increase is particularly noticeable at tropospheric altitudes.

The distribution of CO VMRs below 50 km reflects a completely different seasonal variability because it is not directly affected by CO2 photolysis. During the onset of the GDS, CO mixing ratios are depleted at these altitudes. A similar depletion is also reported by Olsen et al. (2021) from ACS MIR observations. This depletion returned to possibly normal equinoctial abundances after the GDS, until in the southern summer another depletion of CO VMR occurred, around $L_S = 270° - 300°$ (uncertain start in our records due to the lack of TGO observations around $L_S = 265° - 280°$). This occurred in both hemispheres. Although these two periods share a drop in CO VMR, they may not respond to exactly the same processes. The well known increase in CO_2 density in the southern solstice, during the sublimation of the southern polar cap, (Hess et al., 1979; Forget et al., 2008) is surely behind the low CO observed after $L_S = 280°$. However, another mechanism may be at play during very dusty conditions. During the GDS and its decay phase high water vapor abundance has been reported (A. Fedorova et al., 2021; Villanueva et al., 2021; Alday et al., 2021; Belyaev et al., 2021; Brines et al., 2022). This suggests a depletion of CO due to enhanced H_2O which increases the hydroxyl radicals (OH).

At the lowermost altitudes explored, around 20-30 km, the retrieved CO shows large VMR after the GDS in the NH. This increase seems to disappear through the decay phase, and is not observed around $L_S = 270°$. In the SH, however the SO measurements during the onset of the GDS coincides with higher latitudes and a high CO abundance is also seen. This may also disappear as the season advances, but this is not confirmed as our data coverage is incomplete at these low altitudes. Let us bring up here that at the lowermost altitudes the CO sensitivity of our inversion is lower, and climatological effects (*a priori*) may play a role.

At the end of the southern summer, during $L_S = 335° - -354°$, the CO VMR increases at high latitudes in both hemispheres. This enhancement is due to the downwelling branch of the equinoctial hemispheric Hadley cells (Forget et al., 1999; Neary &

This article is protected by copyright. All rights reserved.

Accepted Article

21699100, ja, Downloaded from https://agupubs.onlinelibrary.wiley.com/doi/10.1029/2022JE007282 by The Open University, Wiley Online Library on [23/02/2023]. See the Terms and Conditions (https://onlinelibrary.wiley.com/terms-and-conditions) on Wiley Online Library for rules of use; OA articles are governed by the applicable Creative Commons License

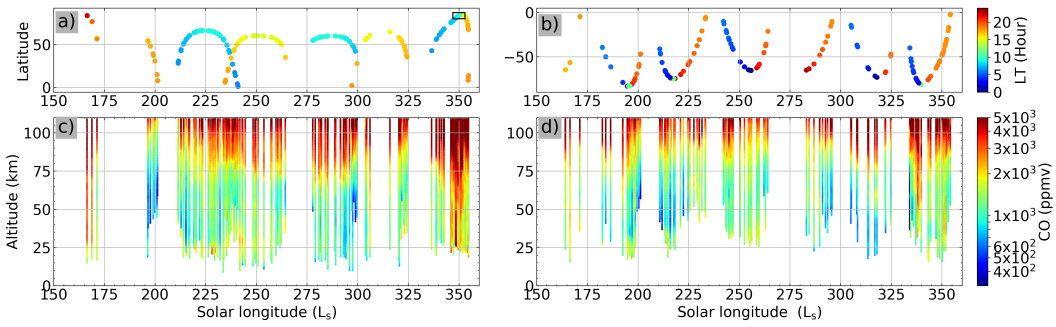

Figure 7. All CO profiles retrieved for this study. Panels a and b show the seasonal and latitudinal distribution of the dataset used, with the colors on scale indicating the localtime. The bottom panels show L_S-altitude distribution of the CO profiles corresponding to the location shown in the top panels. Colors are selected to facilitate inspection of iso-contours, like the orange iso-contour of 2500 ppm, which varies through the seasons (see text for details). A box has been included in panel (a) to indicate the position of the data selected for the study of local time effects (see text)

Daerden, 2018). This enhancement in CO is consistent with a higher column abundance observed in a nadir geometry by the NOMAD LNO channel (Smith et al., 2021).

5.2 Latitudinal Variation

In Figures 8 and 9 we show the latitudinal variation of the CO profiles retrieved from NOMAD-SO and simulated with the PCM, respectively. The CO mixing ratios simulated by the Mars PCM are shown in order to illustrate both the departure from the *a priori* and the predicted dynamical effects on the distribution. According to the PCM simulation, two Hadley cells exist, rising air from the equator and moving to high latitudes in both hemispheres during the two equinoxes, in early northern spring and fall. The ascending branch of the Hadley cells shifts according to the season, as the heating in the subsolar point moves over the planetary surface (Read et al., 2015). During soltices, one of the Hadley branches becomes an intense cross-hemispheric cell, particularly strong during the southern summer solstice ($L_S = 270° - 300°$) (Forget et al., 1999).

Each panel of the Figures 8 and 9 corresponds to a fixed season indicated at the top of each panel. These eight periods include the onset of the dust storm ($L_S = 190° - -205°$), the decaying phase of the GDS ($L_S = 210° - -225°$), the initial phase of the

This article is protected by copyright. All rights reserved.

Accepted Article

21699100, ja, Downloaded from https://agupubs.onlinelibrary.wiley.com/doi/10.1029/2022JE007282 by The Open University, Wiley Online Library on [23/02/2023]. See the Terms and Conditions (https://onlinelibrary.wiley.com/terms-and-conditions) on Wiley Online Library for rules of use; OA articles are governed by the applicable Creative Commons License

perihelion season ($L_S = 240° - -250°$), the late phase of perihelion ($L_S = 250° - -265°$), and some periods of the southern summer ($L_S = 285° - -300°$, $L_S = 300° - -315°$, $L_S = 316° - -330°$ and $L_S = 331° - -345°$).

During the period $L_S = 190° - -205°$ (Figures 8 and 9, panel a), the Martian dynamics is dominated by two Hadley cells increasing the CO mixing ratios at higher latitudes in both northern and southern hemispheres. In particular, the high mixing ratios found around 25 km over the southern polar latitudes seem to be the result of such a transport. A similar increase in CO VMR amount over the high northern latitudes has also been found by Olsen et al. (2021) during the equinox period.

As the season advances, the CO distributions in panels c, d, e, and f, show variations that can be related to slowly varying solar driven CO_2 photolysis at high altitudes (González-Galindo et al., 2009) and to a Hadley circulation pattern with an ascending flux which is evolving through these periods. The latitudinal gradient in the CO VMR above $\sim$ 70 km vary with the seasons, as can be seen from the changes between panels. Around perihelion, the changes between adjacent panels c and d of Figures 8 and 9 are too short in time for a significant change in solar isolation. One possibility is that these are due to large scale transport. We cannot exclude also small scale variations, including measurement noise and thermal effects in the background atmosphere, for which CO VMR is very sensitive. At tropospheric altitudes, there are also changes which seem to be linked to water vapor. We know water vapor presents significant variations in the lower atmosphere, and in particular in these seasons is lower than the amount observed during the GDS (Aoki et al., 2019; A. A. Fedorova et al., 2020; Brines et al., 2022). Unfortunately, we do not have homogeneous nor symmetric coverage in latitudes between both hemispheres during this key period that includes the perihelion and the southern summer solstice. CO seems to be an excellent tracer to characterize this season but more insightful analysis requires the use of GCM simulations or data assimilation.

During $L_S = 285° - -300°$ and $L_S = 300° - -315°$ (panels e and f in Figure 8), a fully developed global inter-hemispheric circulation can be seen in the CO distribution. The latitudinal coverage is patchy and we should rather claim that the distribution observed is compatible with such a global cross-hemispheric pattern, more neatly shown with model simulations (Daerden et al., 2019; Olsen et al., 2021). With this caution in mind, the downwelling branch in the NH seems to be at around 60°N, and seems to reach

This article is protected by copyright. All rights reserved.

Accepted Article

21699100, ja, Downloaded from https://agupubs.onlinelibrary.wiley.com/doi/10.1029/2022JE007282 by The Open University, Wiley Online Library on [23/02/2023]. See the Terms and Conditions (https://onlinelibrary.wiley.com/terms-and-conditions) on Wiley Online Library for rules of use; OA articles are governed by the applicable Creative Commons License

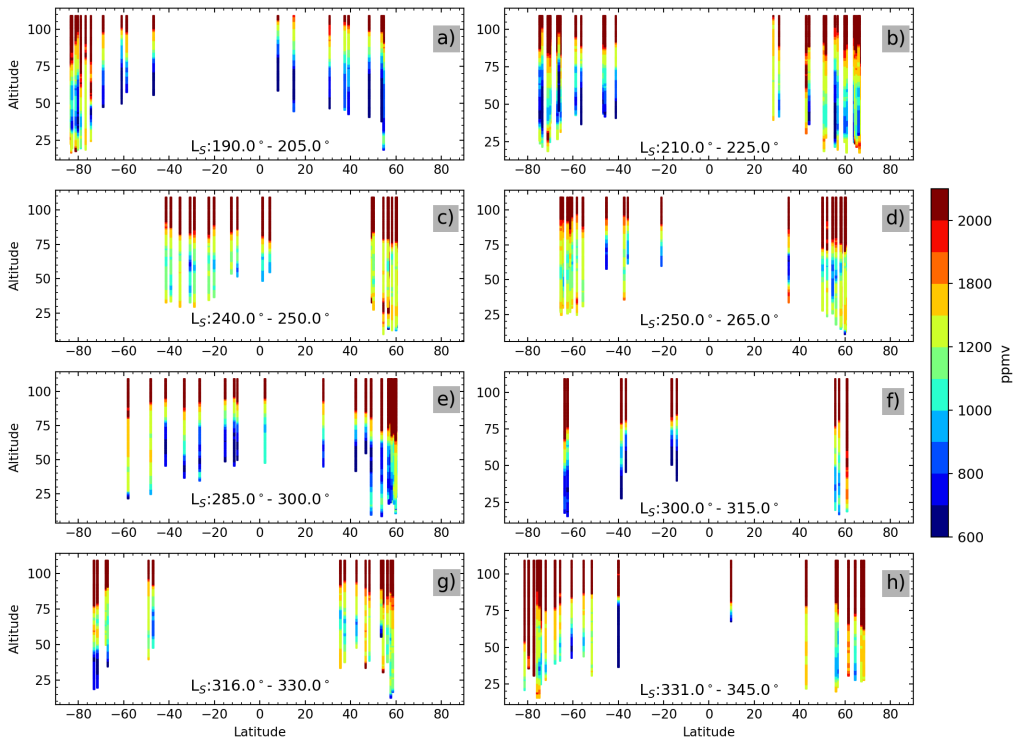

Figure 8. Latitudinal distribution of the retrieved CO profiles after grouping the results in 8 Ls intervals, as indicated in each panel. The color scale indicates the CO VMR values in ppmv.

down to lower tropospheric altitudes, 20-25 km, layers which seem to be enriched in CO compared to lower latitudes. We notice that during this season the distribution from the PCM shows a lower enrichment in CO, which indicates a weaker downwelling in the model. Over 60°N, downwelling of the PCM CO seems to reach only around altitude $\sim$ 55 km increasing the VMR values $>$ 1000 ppm while in the next panel (Figure 9, panel f) the downwelling seems to increase and reach the altitudes around 40 km and VMR values around $\sim$ 900 ppm.

At low altitudes, the TGO mapping is incomplete but low CO amounts are clearly observed at mid-low latitudes (50S-50N) from the beginning of the perihelion season (panel d in Figure 8). This low abundance is maintained or slightly increased during the southern summer (panels e-f). Later on, at the end of southern summer / northern fall, observations by TGO at higher latitudes were possible again (panels g and h in Figure 8). The CO abundance seems to increase there, possibly as a result of dynamics, following downwelling in both hemispheres. Also, the amount of water vapor is decreasing, specially in the NH (A. Fedorova et al., 2021), which may add to the CO increase. In the

This article is protected by copyright. All rights reserved.

Accepted Article

21699100, ja, Downloaded from https://agupubs.onlinelibrary.wiley.com/doi/10.1029/2022JE007282 by The Open University, Wiley Online Library on [23/02/2023]. See the Terms and Conditions (https://onlinelibrary.wiley.com/terms-and-conditions) on Wiley Online Library for rules of use; OA articles are governed by the applicable Creative Commons License

Accepted Article

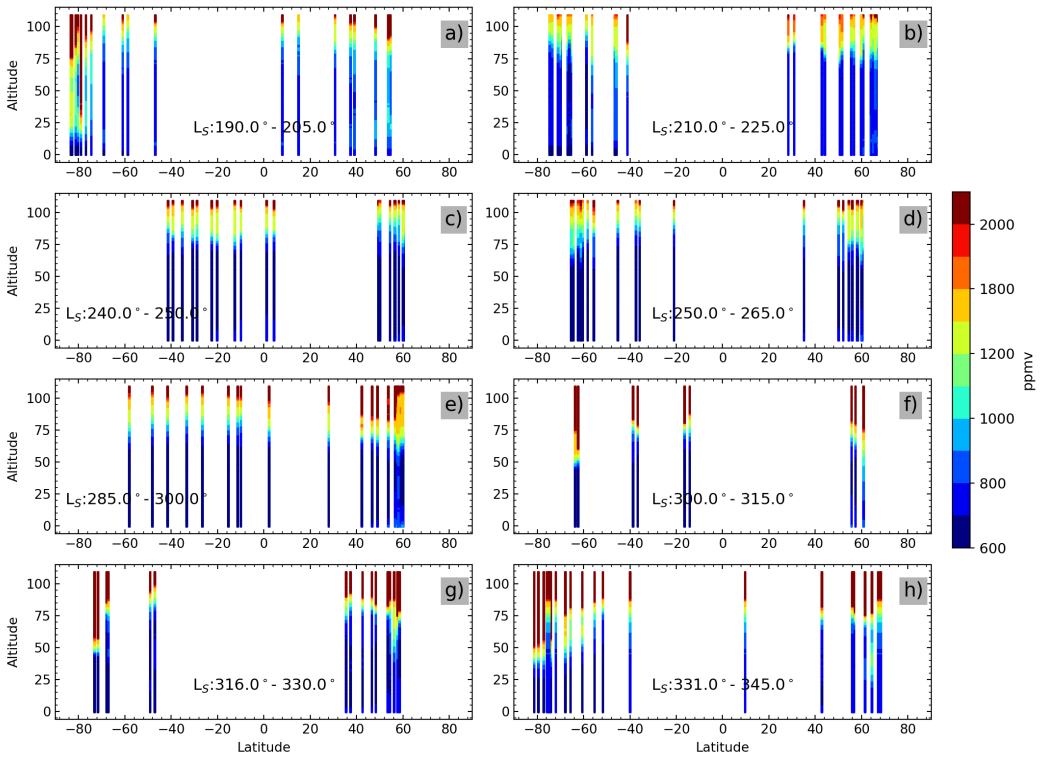

Figure 9. Latitudinal distribution as in Figure 8 but for the PCM CO, using the same set of 8 Ls intervals, as indicated in each panel. The color scale indicates the CO VMR values in ppmv.

This article is protected by copyright. All rights reserved.

21699100, ja, Downloaded from https://agupubs.onlinelibrary.wiley.com/doi/10.1029/2022JE007282 by The Open University, Wiley Online Library on [23/02/2023]. See the Terms and Conditions (https://onlinelibrary.wiley.com/terms-and-conditions) on Wiley Online Library for rules of use; OA articles are governed by the applicable Creative Commons License

period shown in panels g and h we observe the largest CO over the North polar region. Such variations of the low altitude carbon monoxide cannot be seen in the PCM simulations (Figure 9). The PCM CO VMR between 20 and 40 km show small variations compared to that observed in the NOMAD SO observations.

5.3 Diurnal Variations

Given the mixtures of latitudes, seasons, and local times, it is not straightforward to separate them to highlight possible diurnal variations. The L_S spread of the morning (or the evening) observations over NH (see Figure 7 a) are twice as long as the extent of these observations over SH (see Figure 7 b). Also, note that for a given L_S range, NH observations are taken in the morning while SH observations are taken in the evening and vice-versa. We looked for locations where both latitude and L_S have small variations, but only found cases at very high latitudes. Here we examine the retrieved profiles within the box indicated in Figure 7 panel a, which extends in L_S from 347° to 353° and in latitudes from 80°N to 86°N. The results are shown in Figure 10. Analysis of diurnal cycles at such high latitudes requires cautions, specially during equinox conditions, when the axial tilt is perpendicular to the sun. Trace mixing ratios in polar regions are very affected by global dynamics, hence some variations may not be necessarily diurnal. In addition, there can be an effect due to the L_S variation within our box, because at very high latitudes and close to equinox, an L_S range of only 6° (about a week long) represents significant changes in the illumination conditions.

The CO VMR in Figure 10 shows a decrease with local time as well as with L_S below about 60 km. However, we cannot confirm this relation based only on this observation. As mentioned above the period of time described by this figure lies at the end of the northern polar night, approaching equinox. Therefore, most likely this variation is rather related to either downwelling within a polar vortex or to variations in the thermal structure or a combination of both. The polar vortex is particularly strong during Martian winter conditions but such an isolated region can also be formed near equinoxes (Mitchell et al., 2015; Toigo et al., 2017; Streeter et al., 2021). The decrerase in the CO VMR with L_S may also indicate breaking of the polar vortex.

In Figure 10 we observe two peculiar profiles whose VMR values are quite large below about 45 km. These correspond to the latitudes 80.5°N and 80.9°N and, again, there

This article is protected by copyright. All rights reserved.

Accepted Article

21699100, ja, Downloaded from https://agupubs.onlinelibrary.wiley.com/doi/10.1029/2022JE007282 by The Open University, Wiley Online Library on [23/02/2023]. See the Terms and Conditions (https://onlinelibrary.wiley.com/terms-and-conditions) on Wiley Online Library for rules of use; OA articles are governed by the applicable Creative Commons License

are a few plausible explanations of this result, although none of them is completely satisfactory. One possibility is descending CO-rich air within a displaced polar vortex. However, the two locations might require the vortex to be split, as they are not closely placed, and this is not a common situation in Mars (Mitchell et al., 2015). A second possibility is associated to extremely cold patches, near the CO_2 condensation temperature. In such an instance, there should follow an increase in the relative abundance of CO. For this purpose we have examined the individual temperature and density profiles obtained from the NOMAD data by our team down to about 26 km (López Valverde et al., 2022). They are shown in the right panel of Figure 10. The retrieved temperature below about 20-25 km should not be trusted due to low signal (they are merged to the PCM *a priori*), but in the altitudes where the CO VMR is high the temperatures are not particularly extreme, a result which certainly does not support this cold-patch hypothesis. Still, this does not completely rule out the possibility of a stronger CO_2 condensation in those two profiles, because such process might happen at lower altitudes, near the Martian surface, which cannot be seen in our data. We should turn to a third possibility, which is some unknown bias in the inversion. This is not a fully satisfactory explanation either, since we do not observe any peculiarity in the residuals, nor in the retrieval performance (convergence, AKs) of these two profiles. In our opinion, these peculiar CO VMR profiles demand more observations at high latitudes, analyzing NOMAD data collected during more Mars Years, which is an ongoing work in our team.

5.4 Comparison with PCM Simulation

Figures 11 and 12 show comparisons between the CO distribution from the Mars PCM and our retrieved values. For each NOMAD SO scan, a CO VMR profile was extracted from the model at the exact latitude, longitude, local time, and L_S of the occultation path at 50 km altitude, i.e., approximately at the scan's midpoint.

Figure 11 shows the same trend in the vertical distribution of CO in both sets, with a relative abundance increasing with altitude. The scans are shown in colors following the solar longitude, but without distinction among latitudes or hemispheres. This permits a quick visual realization of the global increase in CO VMR with season at high altitudes, between $L_S = 170°$(blue profiles) and $L_S = 350°$ (dark red). However, in the NOMAD VMR, the vertical positive gradient is particularly strong above 60 km, while in the PCM some profiles present steep gradients also at tropospheric altitudes. The re-

This article is protected by copyright. All rights reserved.

Accepted Article

21699100, ja, Downloaded from https://agupubs.onlinelibrary.wiley.com/doi/10.1029/2022JE007282 by The Open University, Wiley Online Library on [23/02/2023]. See the Terms and Conditions (https://onlinelibrary.wiley.com/terms-and-conditions) on Wiley Online Library for rules of use; OA articles are governed by the applicable Creative Commons License

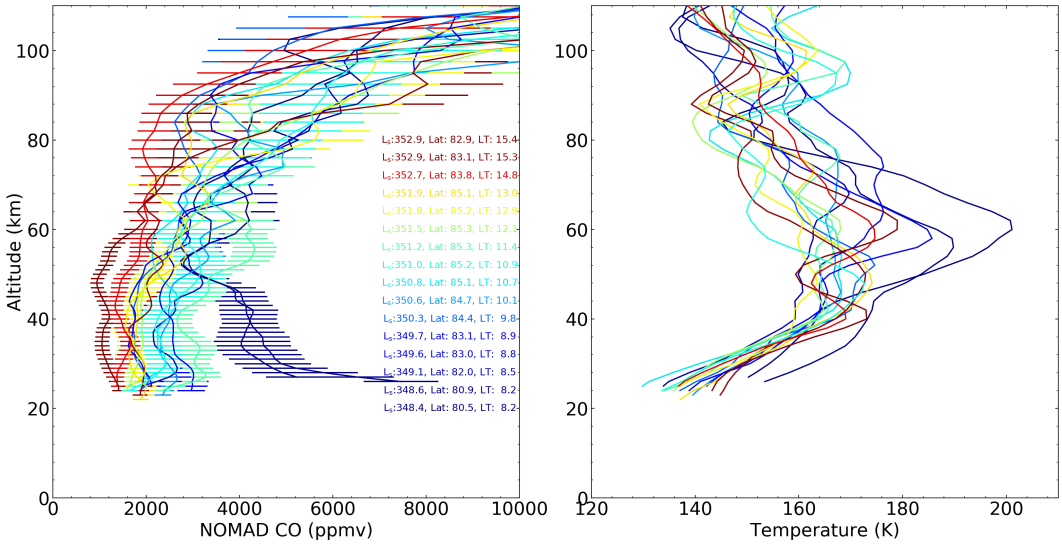

Figure 10. Left panel: variation of CO profiles with local time within a small latitudinal and seasonal box of ranges Lat = 80°-85° and L_S = 347° - 353°. The color of the curves indicate the local time of the observations. Location and local time are indicated by the in-box text with the same color. Right panel: retrieved temperatures from NOMAD data associated to each of the CO profiles in the left panel. Temperatures below 20-25 km are not trusted due to low signal. See text for details.

trieved profiles show small scale variations consistent with the measurement noise but also larger oscillations not observed in the PCM data. Similar larger oscillations are also found in the retrieved temperature profiles (López Valverde et al., 2022) compared to the PCM values. We think this may indicate larger dynamical activity than in the model in the form of thermal tides and gravity waves.

Further insights into the NOMAD-PCM comparison can be obtained with Figure 12. This shows that the PCM global distribution and our retrievals agree well. Particularly, the seasonal behavior of the CO VMR above $\sim$ 60 km is similar in both distributions. However, some differences can be seen and are highlighted next. First, the PCM CO abundances are globally lower than the NOMAD retrievals at all altitudes, especially in the mesosphere (above 60 km). There are exceptions to this rule, especially at low altitudes, which are evident in Figure 11. Secondly, the two equinox periods show significant differences. During the northern autumn equinox period, L_S = 160°– 180°, mixing ratios lower than the PCM are observed at high latitudes. A similar result was obtained by Olsen et al. (2021) from their model-data comparisons. The agreement between

This article is protected by copyright. All rights reserved.

Accepted Article

21699100, ja, Downloaded from https://agupubs.onlinelibrary.wiley.com/doi/10.1029/2022JE007282 by The Open University, Wiley Online Library on [23/02/2023]. See the Terms and Conditions (https://onlinelibrary.wiley.com/terms-and-conditions) on Wiley Online Library for rules of use; OA articles are governed by the applicable Creative Commons License

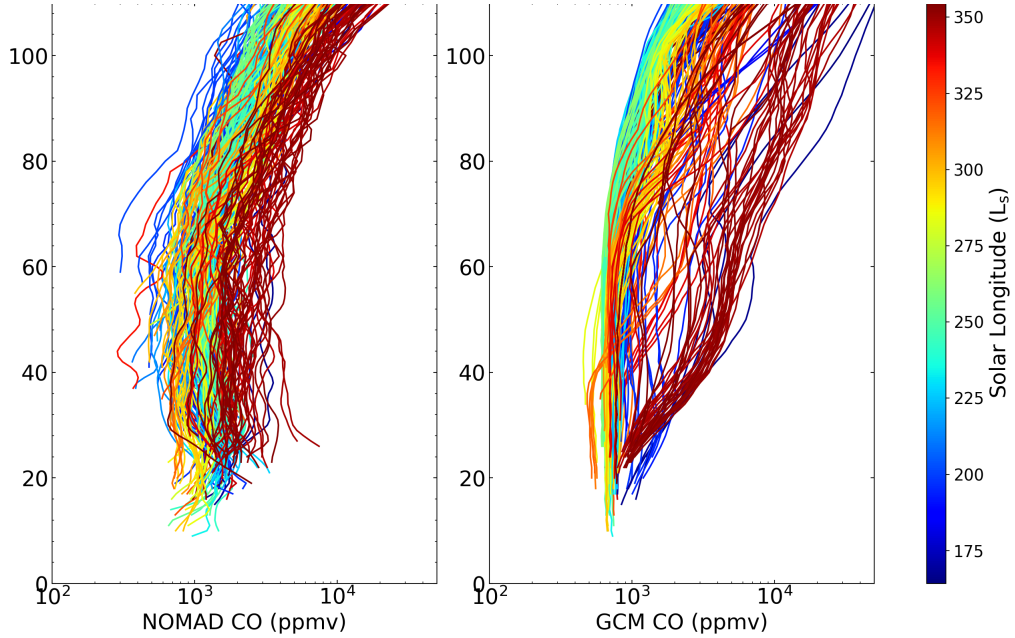

Figure 11. Comparison of the whole set of retrieved NOMAD CO VMR profiles (left panel) with the PCM results (right-hand side panel). The color scale indicates the solar longitude of the scans.

model and data seems better at lower-mid latitudes and in both hemispheres, although not many profiles are available in this period to support this idea. In the other equinox period, during $L_S = 345° - 354°$, the retrieved CO is lower than the PCM in the NH by at least a factor of 2 while the opposite is observed in the SH.

Among other differences, the PCM maps do not show a depletion of CO during the onset and decay phases of the GDS as strong as in the NOMAD results. However, in this period, comparatively a better quantitative agreement is obtained between the *a priori* and the retrieved CO. The modelled water vapor and temperatures are also in better agreement with the retrieved water vapor (Brines et al., 2022) and the retrieved temperature (López Valverde et al., 2022). A last significant difference is observed around $L_S = 315°$ at altitudes between 60 and 80 km. This corresponds to southern high latitudes, where both distributions show a large CO abundance at mesospheric altitudes, driven by an active global circulation, but it is larger in the PCM by a factor 3-5.

This article is protected by copyright. All rights reserved.

Accepted Article

21699100, ja, Downloaded from https://agupubs.onlinelibrary.wiley.com/doi/10.1029/2022JE007282 by The Open University, Wiley Online Library on [23/02/2023]. See the Terms and Conditions (https://onlinelibrary.wiley.com/terms-and-conditions) on Wiley Online Library for rules of use; OA articles are governed by the applicable Creative Commons License

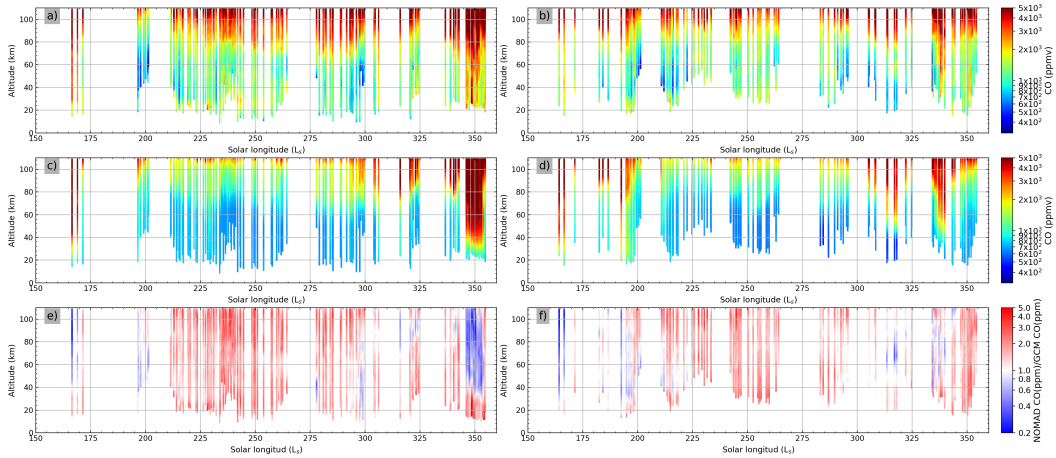

Figure 12. Comparison of PCM CO densities with the retrieved ones. The top panels a and b show the retrieved CO VMR. Panels c and d show the PCM CO mixing ratios and panels e and f show the ratios NOMAD/PCM. Left panels (a, c, and e) correspond to the NH and right panels (b, d, and f) to the SH.

6 Comparison with Previous Results

Figure 13 shows a comparison of our CO vertical profiles with the profiles retrieved from ACS observations (Olsen et al., 2021). The ACS and SO profiles observed within a box of 5° latitude and 5° L_S are chosen for the comparison. From the 32 profiles studied by Olsen et al. (2021), 17 were selected for this comparison. Since the ACS and SO observations are not exactly collocated and they are processed with two very different retrieval schemes, some differences in the CO densities are expected. Profiles in panels b, c, & d show the CO densities during the onset of the GDS. The results from the both instruments compare well although our retrieved values are lower than those from ACS below 80 km. The average of the differences, in the range between the lowermost available altitude and 75 km, are 225 and 250 ppm in panel b, 306 ppm in panel c and 308 ppm in panel d. During the high dust loading period, however, the average difference is lower, within 150 - 200 ppm (for panels e to j). The highest average difference can be seen over the northern high latitudes during the equinox and reaches 850 - 1200 ppm (panel a).

A major difference among these profiles is to be noted above 80 km where an increase in VMR is usually observed, due to photochemical production. Our values start to increase above 80 km whereas the ACS values start increasing above 100 km. Let us

This article is protected by copyright. All rights reserved.

Accepted Article

21699100, ja, Downloaded from https://agupubs.onlinelibrary.wiley.com/doi/10.1029/2022JE007282 by The Open University, Wiley Online Library on [23/02/2023]. See the Terms and Conditions (https://onlinelibrary.wiley.com/terms-and-conditions) on Wiley Online Library for rules of use; OA articles are governed by the applicable Creative Commons License

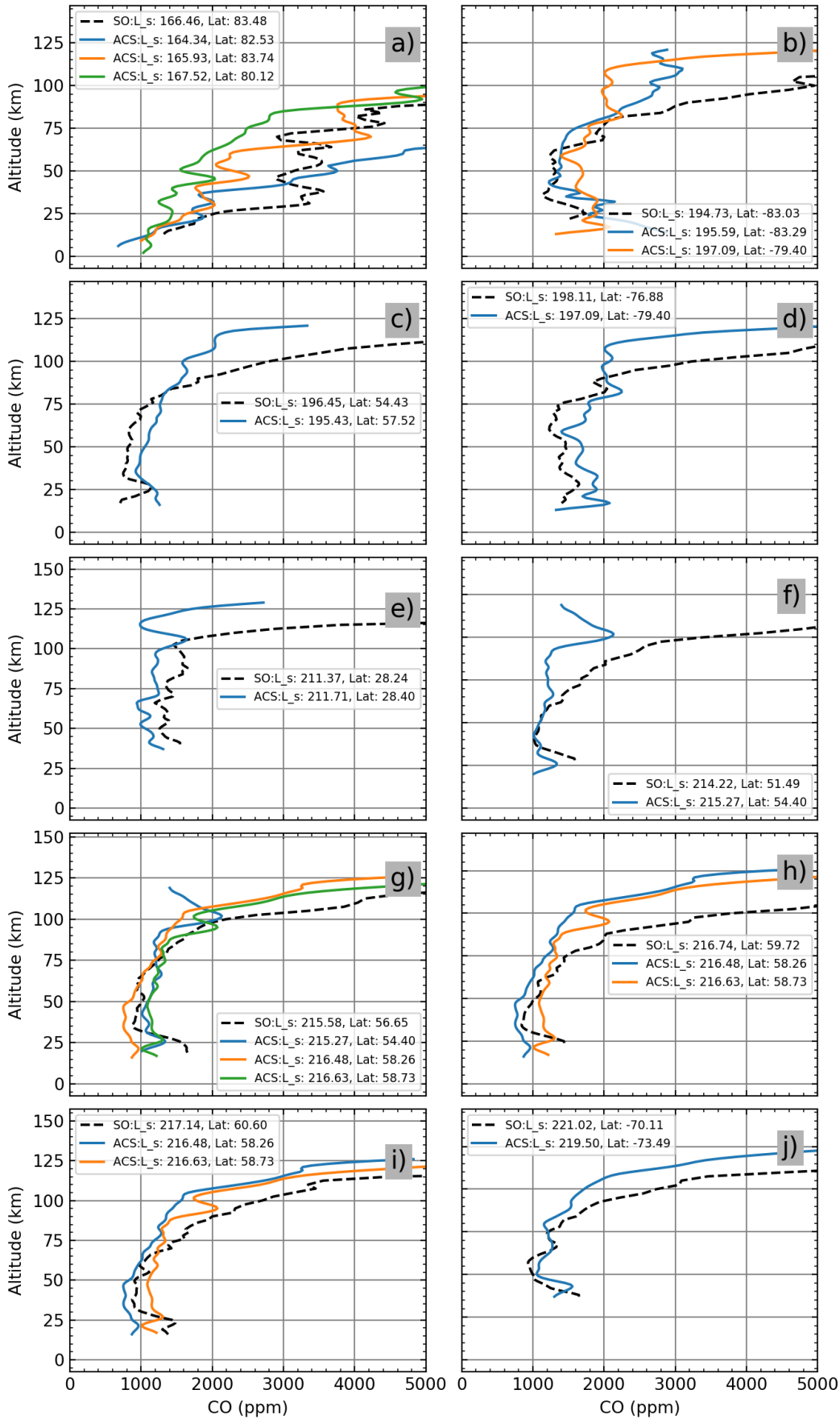

Figure 13. Comparison of the CO profiles in this study with the CO profiles obtained from ACS observations (Olsen et al., 2021). The common profiles within the Lat-L_S box of dimension $5° \times 5°$ are compared.

This article is protected by copyright. All rights reserved.

Accepted Article

21699100, ja, Downloaded from https://agupubs.onlinelibrary.wiley.com/doi/10.1029/2022JE007282 by The Open University, Wiley Online Library on [23/02/2023]. See the Terms and Conditions (https://onlinelibrary.wiley.com/terms-and-conditions) on Wiley Online Library for rules of use; OA articles are governed by the applicable Creative Commons License

recall that at these high altitudes the measurements are particularly noisy, even in the temperature retrievals, and both ACS MIR and NOMAD SO present the largest uncertainties. Apart from these differences, and as mentioned above, our CO VMR results compare well with the ACS profiles, the differences between them arising most likely from different thermal structures and differences in retrieval methods. This is a first comparison intended to illustrate the need of a further, more in-depth, and coordinated comparison between both instruments.

Other instruments from the Mars orbit and ground-based observations have provided column abundances of CO. These columnar mixing ratios are obviously representative of the CO abundance near the planet's surface. In our retrieved profiles, the lowest altitude of sounding is variable depending on atmospheric dust loading, but is above 20 km in most solar ocultation scans. The amount of CO in a column below our lowermost altitude is between 5 and 50 times the amount of CO above. In order to compare with previous nadir measurements, instead of CO column mixing ratios, we have calculated mean VMRs of our retrieved CO profiles. These are computed from the lowermost retrieved altitude up to 60 km, averaging these in the L_S bins of Figure 8 and comprising all the latitudes between 45°N and 45°S. The global average value obtained is 884 ppm. This compares well with LNO and PFS global averages, which are 800 ppm (Smith et al., 2021) and 820 ppm (Bouche et al., 2021) respectively. The global average values obtained from ACS NIR and MIR is 970 ppm (A. Fedorova et al., 2022) which is 9% higher than our values. Therefore, in terms of global averages, our VMRs are comparable with the previous results. During the GDS, however, we obtained a lower average VMR, of 619 ppm, while the LNO and PFS nadir data do not show this depletion. Both MIR and NIR also found an averaged depletion in ths period. In another period that we analyzed, during the southern summer around $L_S = 270° - 300°$, our values are around 900 ppm, which is higher than the column measurements by LNO and CRISM but agree well with NIR and MIR results. Our averaged binned values also seem to agree with NIR and MIR at the end of the MY34, with average VMR around 800-850 ppm.

7 Summary and Conclusions

For the first time, we have retrieved Martian CO density profiles up to about 100 km tangent altitudes from the NOMAD solar occultation channel for MY 34 between $L_S = 160°--354°$ using collocated retrievals of temperatures and pressures. The two main

This article is protected by copyright. All rights reserved.

Accepted Article

21699100, ja, Downloaded from https://agupubs.onlinelibrary.wiley.com/doi/10.1029/2022JE007282 by The Open University, Wiley Online Library on [23/02/2023]. See the Terms and Conditions (https://onlinelibrary.wiley.com/terms-and-conditions) on Wiley Online Library for rules of use; OA articles are governed by the applicable Creative Commons License

sources of uncertainty in our results come from the variability in the AOTF transfer function and from the temperatures. The retrieval errors are typically lower than 10% below 80km which can grow up to 30% above this altitude. Below 80 km the vertical resolution is usually better than 5 km.

The distribution of CO abundances observed by NOMAD globally agrees with latitudinal and seasonal variations obtained before with nadir observations, made by spacecraft instruments like CRISM (Smith et al., 2009), PFS (Sindoni et al., 2011) and NOMAD-LNO nadir sounding (Smith et al., 2021). Our retrieved CO mixing ratios agree well with the retrieved CO mixing ratios from ACS observations. The agreements are strikingly well during the onset and decay period of the GDS. The agreement with ACS results during the equinox period over northern high latitudes is also good regarding the sharp increase in VMR values with altitude, which was obtained with both the instruments (Figure 13).

We find a strong depletion in CO VMRs during the onset of GDS which is more pronounced over the NH. This was also reported by Olsen et al. (2021), who mentioned a possible explanation, related to the amount of H_2O. During the dust storm season, the atmospheric water vapor increases, and therefore the OH radicals, which causes this depletion. We think this may indeed be one of the reasons, and below we describe the period, southern summer, where we also observe links between the H_2O and CO abundances.

We observe an enhancement in CO at altitudes around 25 km over the southern hemisphere during the onset of the GDS. We attribute this enhancement to the downwelling branch of the southern Hadley cell (bringing down mesospheric air, enriched in CO, as detailed in section 5.2). However, a different increase in the CO densities is found over the northern hemisphere from low to mid latitudes during the decay phase of the GDS. In contrast to the previous one, this enhancement could rather be dominated by the lack of OH radicals following the decrease of incoming solar radiation.

The seasonal behavior of CO profiles reveals that CO VMRs below 60 km decrease during the southern summer all over the globe. This decrease may respond to a combination of effects. One of these can be the release of CO_2 and H_2O from the southern polar cap during this season (Forget et al., 2008). Increase of CO VMR at these altitudes is only found at the beginning of southern spring and the end of southern summer.

This article is protected by copyright. All rights reserved.

Accepted Article

21699100, ja, Downloaded from https://agupubs.onlinelibrary.wiley.com/doi/10.1029/2022JE007282 by The Open University, Wiley Online Library on [23/02/2023]. See the Terms and Conditions (https://onlinelibrary.wiley.com/terms-and-conditions) on Wiley Online Library for rules of use; OA articles are governed by the applicable Creative Commons License

Regarding the latitudinal distribution, a couple of distinct periods can be seen in the data. In particular, the period $L_S = 285° - 300°$ shows the impact of the global Hadley circulation. The descending branch of the global Hadley cell lies over 60°N, while the ascending branch is seen in the SH around 40°S. This describes well the known dynamical global pattern on Mars during the southern summer solstice $L_S = 270° - -300°$ (Forget et al., 1999; Read et al., 2015; Neary et al., 2020).

Regarding the comparison with the Mars PCM (our *a priori*) the simulated CO VMRs agree qualitatively with the retrieved CO. A good quantitative agreement between the simulated and the observed CO VMRs is found during the onset of the GDS and during the period around $L_S = 300°$ when the modelled water vapor and temperature are also in better agreement with the retrieved values (López Valverde et al., 2022; Brines et al., 2022). Nonetheless, there are some significant differences. Among the differences with the PCM simulations, our retrieved CO VMR seems to be lower than the model prediction during the beginning of the northern spring over NH. In this season the retrieved CO VMRs are larger over the SH. In general, the retrieved VMRs are higher than the simulated values during $L_S = 210° - 290°$. An important difference was found in the comparison of the latitudinal distributions of CO (Figures 8 and 9), is the presence of a weaker south-to-north transport in the model during the southern summer. The NOMAD SO profiles (Figure 8, panel e) show a larger enrichment of CO mixing ratios over the northern high latitude surely due to a stronger global Hadley cell.

We plan to extend our retrieval approach to the whole NOMAD dataset in order to study CO distribution for a couple of complete Martian years, to compare the CO mixing ratios between years with and without global dust storm, and to gain further insight into seasonal and latitudinal variations in a more complete coverage. This dataset can also be very valuable for PCM modeling and validation purposes. Detailed comparisons with ACS observations of CO are also foreseen.

Appendix A AOTF Characterization

The NOMAD SO measurements are acquired by selecting different diffraction orders, and each datafile corresponds to one order. This is because the AOTF ideally selects one order at a time for diffraction through the grating, and we call it the main diffraction order during that observation. The tuning of the AOTF for whichever main diffrac-

This article is protected by copyright. All rights reserved.

Accepted Article

21699100, ja, Downloaded from https://agupubs.onlinelibrary.wiley.com/doi/10.1029/2022JE007282 by The Open University, Wiley Online Library on [23/02/2023]. See the Terms and Conditions (https://onlinelibrary.wiley.com/terms-and-conditions) on Wiley Online Library for rules of use; OA articles are governed by the applicable Creative Commons License

tion order is set through a radio-frequency input. A typical AOTF tuning relation with wavenumber is given in Neefs et al. (2015). For example, for a radio frequency of 25MHz, the diffraction order 190 is selected. The diffraction efficiency of the AOTF is characterized by a function over the permitted bandpass and is called AOTF transfer function (I. Thomas et al., 2016; Liuzzi et al., 2019). The precise functional of the AOTF is very important to characterize the measurement, and it has been the subject of a recent revision (Villanueva et al., 2022), which proposed an asymmetric sync-squared function characterized by four parameters. The functional and the parameters were determined using what are called mini-scans, i.e., a specific sun observation campaign devoted to fine-tune the channel calibration. As a result of that study, nominal values for those parameters were proposed for each of the NOMAD SO diffraction orders. However, the empirical characterization of the parameters is not perfect, and the uncertainties are particularly large in the spectral region of the CO orders 186-191.

For this reason, CO is one of the hardest targets of the NOMAD SO channel, and it requires a good fine-tuning of its AOTF. In order to gain some insight into this key analysis, we need to analyze further some of the AOTF parameters.

The sinc square AOTF function basically consists of a series of decreasing sidelobes around the main peak, this one laying in the main order while the sidelobes peak in the adjacent orders. The magnitude and shape of the sidelobes is parameterized with the help of an "asymmetry factor" (AF) and a "sidelobes ratio" (SR). As its name suggests, a larger sidelobes ratio increases the relative importance of the sidelobes and decreases the AOTF response in the central lobe, i.e., in the main order. On the other hand, a large asymmetry factor decreases the left lobes and introduces asymmetry between the lobes on both sides. For the detailed discussion on the AOTF parameters, we refer to Villanueva et al. (2022). Our AOTF also allows for a possible non-zero baseline component, which is parameterized as a shallow and wide Gaussian function, which in the spectral region of the CO orders is about 70.71 cm^{-1} wide and has a peak (referred to as Gaussian offset, or GOS hereafter) of 0.2132, for a normalized AOTF in the central lobe.

An extensive analysis using retrievals of full CO profiles was performed in order to fine-tune these parameters, following a perturbation study and looking for a minimization of the retrievals' residuals. For the evaluation of the residuals, we use the goodness of a fit as defined by a χ^2 value (Eq. 3 in Section 4). In addition, the accurate determination of the AOTF parameters should result in similar carbon monoxide densities for

This article is protected by copyright. All rights reserved.

Accepted Article

21699100, ja, Downloaded from https://agupubs.onlinelibrary.wiley.com/doi/10.1029/2022JE007282 by The Open University, Wiley Online Library on [23/02/2023]. See the Terms and Conditions (https://onlinelibrary.wiley.com/terms-and-conditions) on Wiley Online Library for rules of use; OA articles are governed by the applicable Creative Commons License

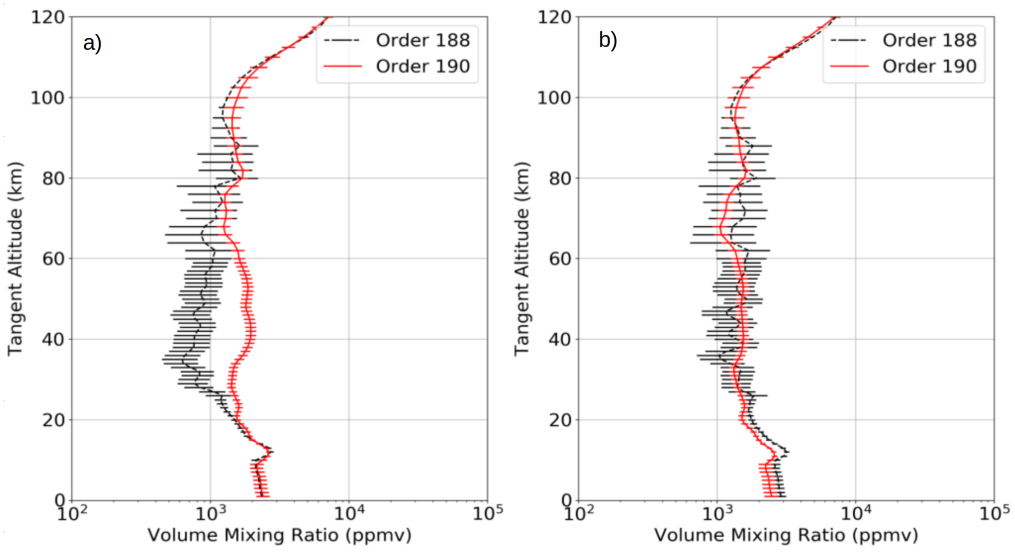

Figure A1. Agreement between the CO profiles from orders 188 and 190 before (panel a) and after (panel b) the fine-tuning of the AOTF parameters for scan *20180907_014655_1p0a_SO_A_I*. In these retrievals a dust filter of opacity 0.5 has been applied which corresponds to an altitude $\sim$ 18 km. This implies no use of measurement below the altitude.

different CO orders due to a more realistic contribution to the CO absorption lines from different orders.

Figure A1 (panel a) shows an example of a CO profile retrieved for one particular scan (*20180907_014655_1p0a_SO_A_I* taken at around 58N and Ls 245) where two different diffraction orders were measured at the same time, orders 188 and 190. In this retrieval, the nominal AOTF parameters were used. The overall agreement between these two CO profiles in the altitude region between 20 and 80 km is not very satisfactory.

In order to make the fine-tuning simple, we started with one of the parameters, in particular the Gaussian offset, or GOS. We chose only the central part of the CO orders, dominated by a relatively small number of CO absorption lines. In the center of a given order, the contribution from that main order is largest compared to other orders' contributions, and the GOS parameter plays the most important role in determining the total contribution (Villanueva et al., 2022). We also selected one scan with low to moderate measurement noise and confined our retrievals to altitudes with low dust opacity (*20180907_014655_1p0a_SO_A_I*, mentioned above). In this scan, a slant optical depth lower than 0.5 means altitudes above 18 km, approximately. We chose a set of values around

This article is protected by copyright. All rights reserved.

Accepted Article

21699100, ja, Downloaded from https://agupubs.onlinelibrary.wiley.com/doi/10.1029/2022JE007282 by The Open University, Wiley Online Library on [23/02/2023]. See the Terms and Conditions (https://onlinelibrary.wiley.com/terms-and-conditions) on Wiley Online Library for rules of use; OA articles are governed by the applicable Creative Commons License

the nominal value GOS=0.2132 proposed by Villanueva et al. (2022) for order 190. Figure A2 shows a comparison among the vertical CO profiles obtained with six different GOS values. The CO VMR in the region between 30 and 80 km is very sensitive to this parameter. The lowest χ^2 was found for values within 0.1 and 0.2. A similar exercise is repeated for order 188. Values of 0.18 for order 188 and 0.2 for order 190 were finally selected as our best Gaussian offsets.

As for the other parameters namely, the asymmetry factor (AF) and the sidelobe ratio (SR), another extensive set of retrievals was performed, once the GOS values were fixed. A table of the χ^2 values obtained from their best fit residuals at the end of the inversions are presented in Figure A3. Similar analysis has been performed to fine-tuning other NOMAD SO orders by our team (see companion papers in this special issue). The closer the χ^2 value to unity the better the fitting of the retrieval (Jurado Navarro et al., 2016). In Figure A3 the region of this parameter space with best χ^2 values, shown in dark blue, occupies a broad diagonal. The values finally selected for this study lie in this diagonal correspond to SR=2.41 and AF=2.31.

Back to Figure A1, the CO VMR obtained with the fine-tuned parameters described here are shown in panel b. They are much closer than with the nominal values from Villanueva et al. (2022) and the differences lie within the errors of the retrieval. We recommend these values and AOTF for any future retrievals of CO from these NOMAD SO orders.

Appendix B Synthetic Retrievals

Synthetic retrievals represent an excellent exercise to analyze the performance of a given retrieval setup and assumptions, like regularization and dependence on a priori climatologies. In this study, synthetic spectra were generated using our forward model KOPRA, and are intended to supply spectra equivalent to the Level 1 calibrated transmittances provided by the NOMAD PI team, but we used a given set of AOTF parameters, therefore avoiding uncertainties from the actual instrument's AOTF. For the same reason, these spectra are free from bending effects and from spectral shifts due to inaccuracies during calibration (see Section 3). The atmospheric pressure and temperature, and the *a priori* CO were obtained from the Mars PCM model. The KOPRA simulations correspond to the precise altitudes of a given scan in order 190. A random noise component with a standard deviation given by the measurement noise in the calibrated datafile was added to the KOPRA simulations.

This article is protected by copyright. All rights reserved.

Accepted Article

21699100, ja, Downloaded from https://agupubs.onlinelibrary.wiley.com/doi/10.1029/2022JE007282 by The Open University, Wiley Online Library on [23/02/2023]. See the Terms and Conditions (https://onlinelibrary.wiley.com/terms-and-conditions) on Wiley Online Library for rules of use; OA articles are governed by the applicable Creative Commons License

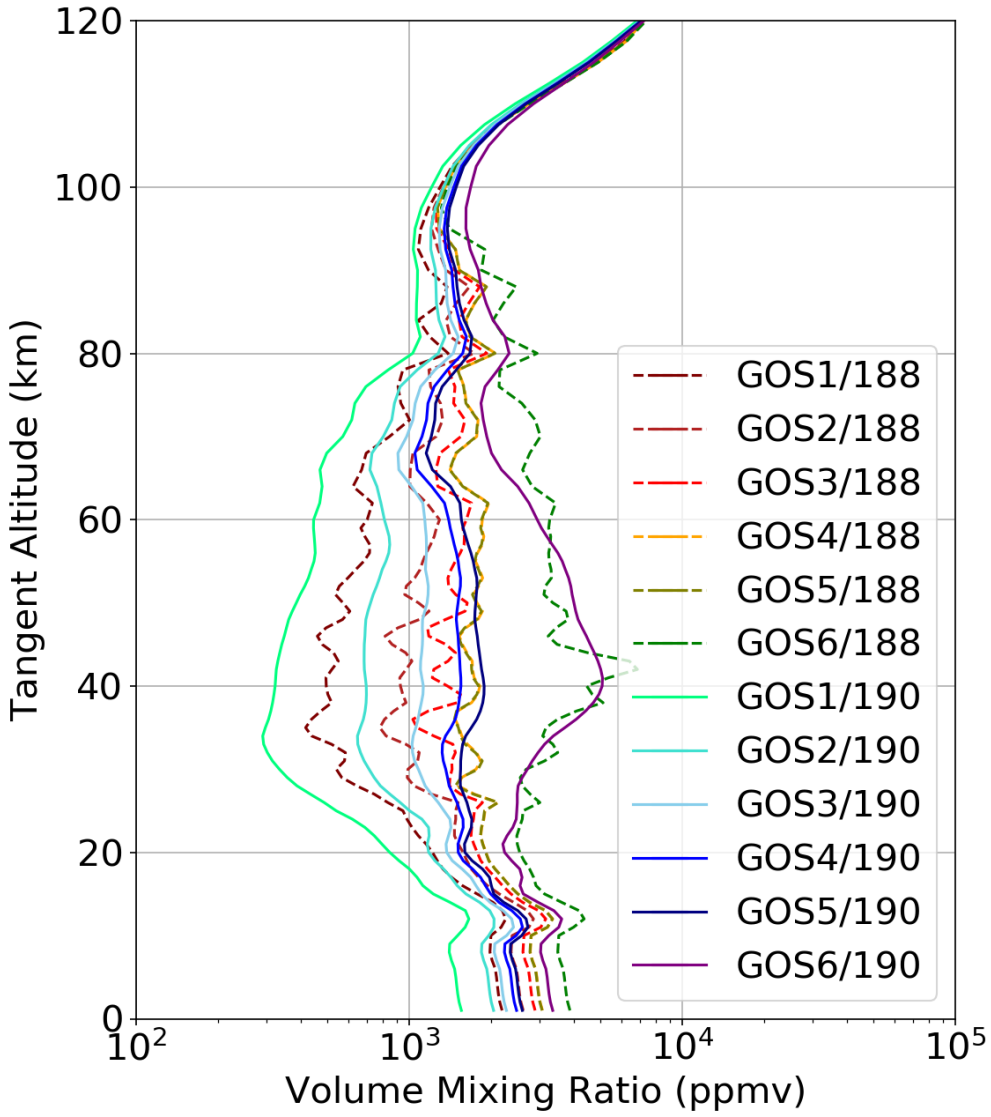

Figure A2. Response of the retrieved CO profiles to variations in the Gaussian offset. GOS1,GOS2,GOS3,GOS4,GOS5, and, GOS6 correspond to values 0.1, 0.15, 0.18, 0.2, 0.3, and 0.35 respectively. The nominal GOS is 0.2132 for order 190. See text for details.

This article is protected by copyright. All rights reserved.

Accepted Article

21699100, ja, Downloaded from https://agupubs.onlinelibrary.wiley.com/doi/10.1029/2022JE007282 by The Open University, Wiley Online Library on [23/02/2023]. See the Terms and Conditions (https://onlinelibrary.wiley.com/terms-and-conditions) on Wiley Online Library for rules of use; OA articles are governed by the applicable Creative Commons License

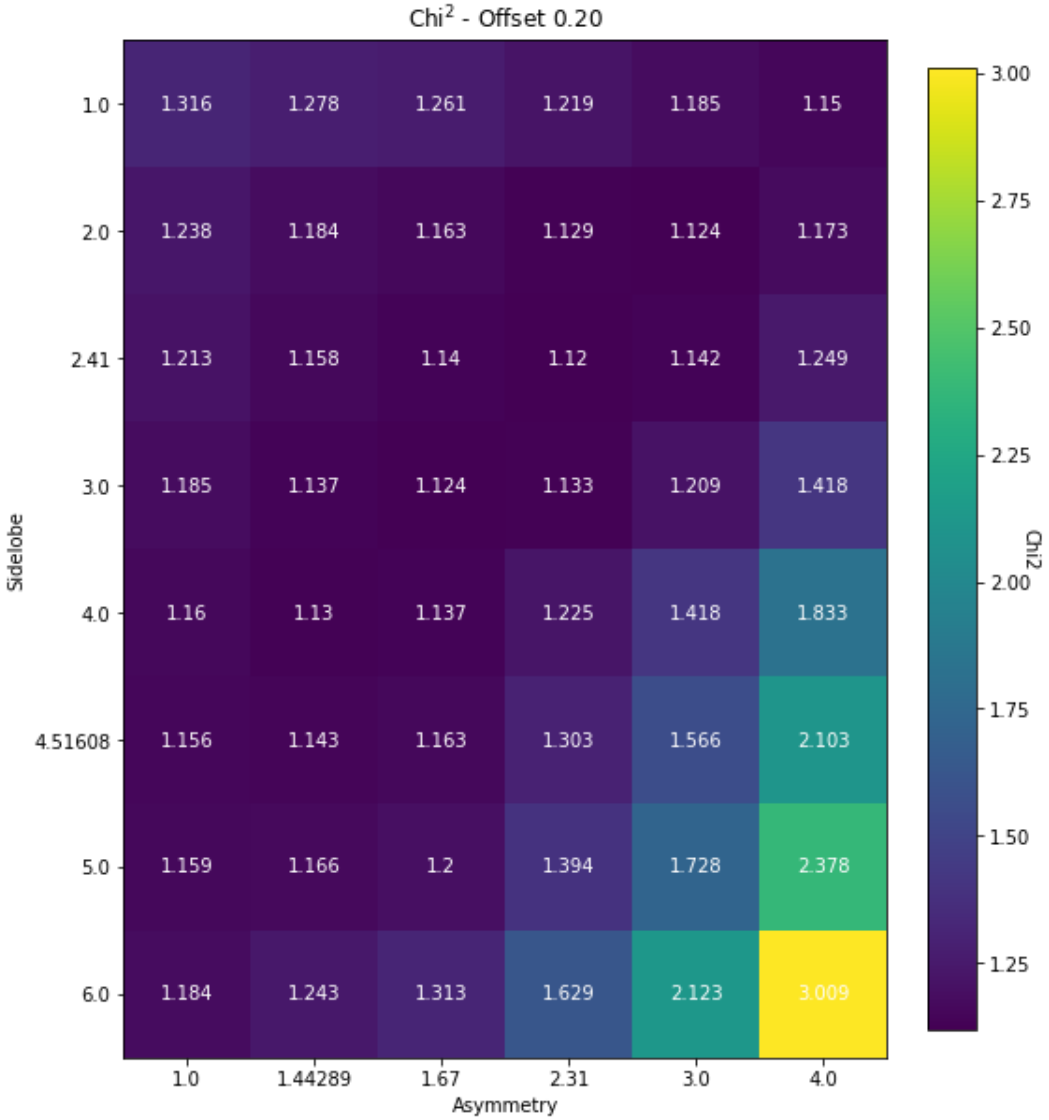

Figure A3. The χ^2 values tabulated for different values of sidelobe ratios and asymmetry factors. The color in the table indicate the values of the χ^2. The lowest χ^2 is obtained for a sidelobe ratio 2.41 and asymmetry factor 2.31.

This article is protected by copyright. All rights reserved.

Accepted Article

21699100, ja, Downloaded from https://agupubs.onlinelibrary.wiley.com/doi/10.1029/2022JE007282 by The Open University, Wiley Online Library on [23/02/2023]. See the Terms and Conditions (https://onlinelibrary.wiley.com/terms-and-conditions) on Wiley Online Library for rules of use; OA articles are governed by the applicable Creative Commons License

Accepted Article

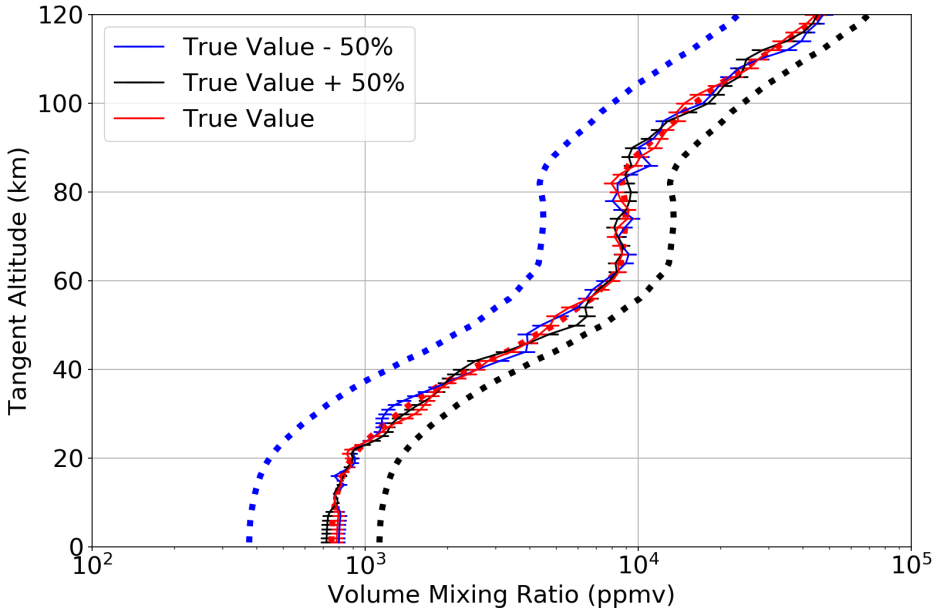

Figure B1. CO profiles retrieved from the synthetic transmittance generated with true value of CO. Colored solid line with errorbar is the retrieved CO with an *a priori* indicated by the dotted line with same color.

This article is protected by copyright. All rights reserved.

21699100, ja, Downloaded from https://agupubs.onlinelibrary.wiley.com/doi/10.1029/2022JE007282 by The Open University, Wiley Online Library on [23/02/2023]. See the Terms and Conditions (https://onlinelibrary.wiley.com/terms-and-conditions) on Wiley Online Library for rules of use; OA articles are governed by the applicable Creative Commons License

In this section, we present a study devoted to test the dependence on the *a priori* CO densities. In Figure B1 we show three CO profiles, from retrievals performed with three different *a priori* CO profiles: (i) the nominal VMR from the GCM, which also represents the "true profile", (ii) the nominal profile reduced by 50% at all altitudes, and (iii) the nominal profile increased by 50% at all altitudes. In the three exercises, the retrieved CO densities essentially coincide among them and with the true profile, with deviations lower than the retrieval errors. Thus, in these conditions, our retrieval scheme gives correct and robust results against *a priori* assumptions.

Acknowledgments

The IAA/CSIC team acknowledges financial support from the State Agency for Research of the Spanish MCIU through the 'Center of Excellence Severo Ochoa' award for the Instituto de Astrofisica de Andalucia (SEV-2017-0709) and funding by grant PGC2018-101836-B-100 (MCIU/AEI/FEDER, EU). F.G.G. is funded by the Spanish Ministerio de Ciencia, Innovación y Universidades, the Agencia Estatal de Investigación and EC FEDER funds under project RTI2018-100920-J-I00 and from grant CEX2021-001131-S funded by MCIN/AEI/ 10.13039/501100011033. ExoMars is a space mission of the European Space Agency (ESA) and Roscosmos. The NOMAD experiment is led by the Royal Belgian Institute for Space Aeronomy (IASB-BIRA), assisted by Co-PI teams from Spain (IAA-CSIC), Italy (INAF-IAPS), and the United Kingdom (Open University). This project acknowledges funding by the Belgian Science Policy Office (BELSPO), with the financial and contractual coordination by the ESA Prodex Office (PEA 4000103401, 4000121493) as well as by UK Space Agency through grants ST/V002295/1, ST/V005332/1 and ST/S00145X/1 and Italian Space Agency through grant 2018-2-HH.0. US investigators were supported by the National Aeronautics and Space Administration. We want to thank M. Vals, F. Momtmessin, F. Lefevre and the broad team suporting the continuous development of the LMD Mars GCM (Mars PCM).

Open Research/Data availability

The HDF5 datafiles of NOMAD SO Level 1a transmittances used in this study are available at European Space Agency (ESA) planetary archive (https://archives.esac.esa.int/psa), and also at the NOMAD data center (https://nomad.aeronomie.be/index.php/data, (I. R. Thomas et al., 2022; Vandaele et al., 2019)

This article is protected by copyright. All rights reserved.

Accepted Article

21699100, ja, Downloaded from https://agupubs.onlinelibrary.wiley.com/doi/10.1029/2022JE007282 by The Open University, Wiley Online Library on [23/02/2023]. See the Terms and Conditions (https://onlinelibrary.wiley.com/terms-and-conditions) on Wiley Online Library for rules of use; OA articles are governed by the applicable Creative Commons License

The retrieved results, presented in this work are archived at the zenodo repository and can be accessed from Ashimananda Modak (2022).

References

Alday, J., Trokhimovskiy, A., Irwin, P. G., Wilson, C. F., Montmessin, F., Lefèvre, F., ... others (2021). Isotopic fractionation of water and its photolytic products in the atmosphere of mars. *Nature Astronomy*, *5*(9), 943–950.

Aoki, S., Daerden, F., Viscardy, S., Thomas, I., Erwin, J. T., Robert, S., ... others (2021). Annual appearance of hydrogen chloride on mars and a striking similarity with the water vapor vertical distribution observed by tgo/nomad. *Geophysical Research Letters*, *48*(11), e2021GL092506.

Aoki, S., Vandaele, A. C., Daerden, F., Villanueva, G. L., Liuzzi, G., Thomas, I. R., ... others (2019). Water vapor vertical profiles on mars in dust storms observed by tgo/nomad. *Journal of Geophysical Research: Planets*, *124*(12), 3482–3497.

Ashimananda Modak. (2022). Retrieval of Martian atmospheric CO vertical profiles from NOMAD observations during the 1st year of tgo operations measurements. *Zenodo*. Retrieved from `https://doi.org/10.5281/zenodo.7268447`

Belyaev, D. A., Fedorova, A. A., Trokhimovskiy, A., Alday, J., Montmessin, F., Korablev, O. I., ... Shakun, A. V. (2021). Revealing a high water abundance in the upper mesosphere of mars with acs onboard tgo. *Geophysical Research Letters*, *48*(10), e2021GL093411.

Billebaud, F., Brillet, J., Lellouch, E., Fouchet, T., Encrenaz, T., Cottini, V., ... others (2009). Observations of CO in the atmosphere of Mars with pfs onboard Mars express. *Planetary and Space Science*, *57*(12), 1446–1457.

Billebaud, F., Crovisier, J., Lellouch, E., Encrenaz, T., & Maillard, J. (1991). High-resolution infrared spectrum of CO on Mars: evidence for emission lines. *Planetary and space science*, *39*(1-2), 213–218.

Bouche, J., Coheur, P.-F., Giuranna, M., Wolkenberg, P., Nardi, L., Amoroso, M., ... Bauduin, S. (2021). Seasonal and spatial variability of carbon monoxide (co) in the martian atmosphere from pfs/mex observations. *Journal of Geophysical Research: Planets*, *126*(2), e2020JE006480.

Brines, A., Lpez-Valverde, M.-A., Stolzenbach, A., Modak, A., Funke, B., Gonzlez-

This article is protected by copyright. All rights reserved.

Accepted Article

21699100, ja, Downloaded from https://agupubs.onlinelibrary.wiley.com/doi/10.1029/2022JE007282 by The Open University, Wiley Online Library on [23/02/2023]. See the Terms and Conditions (https://onlinelibrary.wiley.com/terms-and-conditions) on Wiley Online Library for rules of use; OA articles are governed by the applicable Creative Commons License

Galindo, F., ... Team, N. (2022). Water vapor vertical distribution on Mars during the perihelion season of MY34 and MY35 from ExoMars-TGO/NOMAD solar occultation measurements. *JGR-submitted*.

Clancy, R., Muhleman, D., & Jakosky, B. (1983). Variability of carbon monoxide in the Mars atmosphere. *Icarus*, *55*(2), 282–301.

Clancy, R. T., Wolff, M. J., Whitney, B. A., Cantor, B. A., Smith, M. D., & McConnochie, T. H. (2010). Extension of atmospheric dust loading to high altitudes during the 2001 mars dust storm: Mgs tes limb observations. *Icarus*, *207*(1), 98–109.

Daerden, F., Neary, L., Viscardy, S., Garca Muoz, A., Clancy, R., Smith, M., ... Fedorova, A. (2019). Mars atmospheric chemistry simulations with the gem-mars general circulation model. *Icarus*, *326*, 197-224.

Encrenaz, T., Fouchet, T., Melchiorri, R., Drossart, P., Gondet, B., Langevin, Y., ... Bézard, B. (2006). Seasonal variations of the Martian CO over Hellas as observed by OMEGA/Mars Express. *Astronomy & Astrophysics*, *459*(1), 265–270.

Encrenaz, T., Lellouch, E., Gulkis, S., & Depater, I. (1991). Submillimeter observations of the (3-2) 12co and 13co transitions in the atmosphere of Mars. In *Bulletin of the american astronomical society* (Vol. 23, p. 1214).

Fedorova, A., Montmessin, F., Korablev, O., Lefèvre, F., Trokhimovskiy, A., & Bertaux, J.-L. (2021). Multi-annual monitoring of the water vapor vertical distribution on Mars by SPICAM on Mars express. *Journal of Geophysical Research: Planets*, *126*(1), e2020JE006616.

Fedorova, A., Trokhimovskiy, A., Lefèvre, F., Olsen, K. S., Korablev, O., Montmessin, F., ... others (2022). Climatology of the co vertical distribution on mars based on acs tgo measurements. *Journal of Geophysical Research: Planets*, e2022JE007195.

Fedorova, A. A., Montmessin, F., Korablev, O., Luginin, M., Trokhimovskiy, A., Belyaev, D. A., ... others (2020). Stormy water on Mars: The distribution and saturation of atmospheric water during the dusty season. *Science*, *367*(6475), 297–300.

Forget, F., Hourdin, F., Fournier, R., Hourdin, C., Talagrand, O., Collins, M., ... Huot, J.-P. (1999). Improved general circulation models of the Martian at-

This article is protected by copyright. All rights reserved.

Accepted Article

21699100, ja, Downloaded from https://agupubs.onlinelibrary.wiley.com/doi/10.1029/2022JE007282 by The Open University, Wiley Online Library on [23/02/2023]. See the Terms and Conditions (https://onlinelibrary.wiley.com/terms-and-conditions) on Wiley Online Library for rules of use; OA articles are governed by the applicable Creative Commons License

mosphere from the surface to above 80 km. *Journal of Geophysical Research: Planets*, *104*(E10), 24155–24175.

Forget, F., Millour, E., Bierjon, A., Delavois, A., Fan, S., Lange, L., ... others (2022). Challenges in mars climate modelling with the lmd mars global climate model, now called the mars planetary climate model(pcm). In *Seventh international workshop on the mars atmosphere: Modelling and observations* (p. 1102).

Forget, F., Millour, E., Montabone, L., & Lefevre, F. (2008). Non condensable gas enrichment and depletion in the Martian polar regions. *LPI Contrib*, *1447*, 9106.

González-Galindo, F., Forget, F., López-Valverde, M., Angelats i Coll, M., & Millour, E. (2009). A ground-to-exosphere martian general circulation model: 1. seasonal, diurnal, and solar cycle variation of thermospheric temperatures. *Journal of Geophysical Research: Planets*, *114*(E4).

González-Galindo, F., López-Valverde, M., Angelats i Coll, M., & Forget, F. (2005). Extension of a Martian general circulation model to thermospheric altitudes: Uv heating and photochemical models. *Journal of Geophysical Research: Planets*, *110*(E9).

Gordon, I. E., Rothman, L. S., Hill, C., Kochanov, R. V., Tan, Y., Bernath, P. F., ... others (2017). The hitran2016 molecular spectroscopic database. *Journal of Quantitative Spectroscopy and Radiative Transfer*, *203*, 3–69.

Guzewich, S. D., Lemmon, M., Smith, C., Martínez, G., de Vicente-Retortillo, Á., Newman, C., ... others (2019). Mars science laboratory observations of the 2018/Mars year 34 global dust storm. *Geophysical Research Letters*, *46*(1), 71–79.

Hess, S. L., Henry, R. M., & Tillman, J. E. (1979). The seasonal variation of atmospheric pressure on mars as affected by the south polar cap. *Journal of Geophysical Research: Solid Earth*, *84*(B6), 2923–2927.

Höpfner, M., & Emde, C. (2005). Comparison of single and multiple scattering approaches for the simulation of limb-emission observations in the mid-ir. *Journal of Quantitative Spectroscopy and Radiative Transfer*, *91*(3), 275–285.

Jurado Navarro, Á. A., et al. (2016). Retrieval of CO2 and collisional parameters from the mipas spectra in the earth atmosphere.

This article is protected by copyright. All rights reserved.

Accepted Article

21699100, ja, Downloaded from https://agupubs.onlinelibrary.wiley.com/doi/10.1029/2022JE007282 by The Open University, Wiley Online Library on [23/02/2023]. See the Terms and Conditions (https://onlinelibrary.wiley.com/terms-and-conditions) on Wiley Online Library for rules of use; OA articles are governed by the applicable Creative Commons License

Kakar, R., Walters, J., & Wilson, W. (1977). Mars: microwave detection of carbon monoxide. *Science*, *196*(4294), 1090–1091.

Kaplan, L. D., Connes, J., & Connes, P. (1969). Carbon monoxide in the Martian atmosphere. *The Astrophysical Journal*, *157*, L187.

Krasnopolsky, V. A. (1995). Uniqueness of a solution of a steady state photochemical problem: applications to mars. *Journal of Geophysical Research: Planets*, *100*(E2), 3263–3276.

Krasnopolsky, V. A. (2003). Spectroscopic mapping of Mars co mixing ratio: Detection of north-south asymmetry. *Journal of Geophysical Research: Planets*, *108*(E2).

Krasnopolsky, V. A. (2015). Variations of carbon monoxide in the martian lower atmosphere. *Icarus*, *253*, 149–155.

Lefèvre, F., & Krasnopolsky, V. (2017). Atmospheric photochemistry. *The atmosphere and climate of Mars*, *18*, 405.

Lefèvre, F., Trokhimovskiy, A., Fedorova, A., Baggio, L., Lacombe, G., Määttänen, A., ... others (2021). Relationship between the ozone and water vapor columns on mars as observed by spicam and calculated by a global climate model. *Journal of Geophysical Research: Planets*, *126*(4), e2021JE006838.

Lellouch, E., Paubert, G., & Encrenaz, T. (1991). Mapping of co millimeter-wave lines in Mars' atmosphere: The spatial variability of carbon monoxide on Mars. *Planetary and space science*, *39*(1-2), 219–224.

Liuzzi, G., Villanueva, G. L., Mumma, M. J., Smith, M. D., Daerden, F., Ristic, B., ... others (2019). Methane on Mars: New insights into the sensitivity of CH4 with the NOMAD/exoMars spectrometer through its first in-flight calibration. *Icarus*, *321*, 671–690.

López Valverde, M.-A., Funke, B., Brines, A., Stolzenbach, A., Modak, A., Hill, B., ... others (2022). Martian atmospheric temperature and density profiles during the 1st year of NOMAD/TGO solar occultation measurements. *Journal of Geophysical Research: Planets*, e2022JE007278.

McElroy, M. B., & Donahue, T. M. (1972). Stability of the martian atmosphere. *Science*, *177*(4053), 986–988.

Mitchell, D., Montabone, L., Thomson, S., & Read, P. (2015). Polar vortices on earth and mars: A comparative study of the climatology and variability from

This article is protected by copyright. All rights reserved.

Accepted Article

21699100, ja, Downloaded from https://agupubs.onlinelibrary.wiley.com/doi/10.1029/2022JE007282 by The Open University, Wiley Online Library on [23/02/2023]. See the Terms and Conditions (https://onlinelibrary.wiley.com/terms-and-conditions) on Wiley Online Library for rules of use; OA articles are governed by the applicable Creative Commons License

reanalyses. *Quarterly Journal of the Royal Meteorological Society*, *141*(687), 550–562. doi: https://doi.org/10.1002/qj.2376

Modak, A., Sheel, V., & Lefèvre, F. (2020). Competing pathways in odd oxygen photochemistry of the martian atmosphere. *Planetary and Space Science*, *181*, 104783.

Montabone, L., Forget, F., Millour, E., Wilson, R., Lewis, S., Cantor, B., ... others (2015). Eight-year climatology of dust optical depth on Mars. *Icarus*, *251*, 65–95.

Montabone, L., Spiga, A., Kass, D. M., Kleinböhl, A., Forget, F., & Millour, E. (2020). Martian year 34 column dust climatology from Mars climate sounder observations: Reconstructed maps and model simulations. *Journal of Geophysical Research: Planets*, *125*(8), e2019JE006111.

Navarro, T., Madeleine, J.-B., Forget, F., Spiga, A., Millour, E., Montmessin, F., & Määttänen, A. (2014). Global climate modeling of the martian water cycle with improved microphysics and radiatively active water ice clouds. *Journal of Geophysical Research: Planets*, *119*(7), 1479–1495.

Neary, L., & Daerden, F. (2018). The gem-mars general circulation model for mars: Description and evaluation. *Icarus*, *300*, 458–476.

Neary, L., Daerden, F., Aoki, S., Whiteway, J., Clancy, R. T., Smith, M., ... others (2020). Explanation for the increase in high-altitude water on mars observed by nomad during the 2018 global dust storm. *Geophysical Research Letters*, *47*(7), e2019GL084354.

Neefs, E., Vandaele, A. C., Drummond, R., Thomas, I. R., Berkenbosch, S., Clairquin, R., ... others (2015). NOMAD spectrometer on the exoMars trace gas orbiter mission: part 1design, manufacturing and testing of the infrared channels. *Applied optics*, *54*(28), 8494–8520.

Olsen, K., Lefèvre, F., Montmessin, F., Fedorova, A., Trokhimovskiy, A., Baggio, L., ... others (2021). The vertical structure of CO in the Martian atmosphere from the exoMars trace gas orbiter. *Nature Geoscience*, *14*(2), 67–71.

Parkinson, T., & Hunten, D. (1972). Spectroscopy and acronomy of o 2 on mars. *Journal of Atmospheric Sciences*, *29*(7), 1380–1390.

Patel, M. R., Antoine, P., Mason, J., Leese, M., Hathi, B., Stevens, A. H., ... others (2017). NOMAD spectrometer on the exoMars trace gas orbiter mission:

This article is protected by copyright. All rights reserved.

Accepted Article

21699100, ja, Downloaded from https://agupubs.onlinelibrary.wiley.com/doi/10.1029/2022JE007282 by The Open University, Wiley Online Library on [23/02/2023]. See the Terms and Conditions (https://onlinelibrary.wiley.com/terms-and-conditions) on Wiley Online Library for rules of use; OA articles are governed by the applicable Creative Commons License

part 2design, manufacturing, and testing of the ultraviolet and visible channel. *Applied optics*, *56*(10), 2771–2782.

Read, P., Lewis, S., & Mulholland, D. (2015). The physics of martian weather and climate: a review. *Reports on Progress in Physics*, *78*(12), 125901.

Rodgers, C. D. (2000). *Inverse methods for atmospheric sounding: theory and practice* (Vol. 2). World scientific.

Rodrigo, R., Garcia-Alvarez, E., Lopez-Gonzalez, M., & Lopez-Moreno, J. (1990). A nonsteady one-dimensional theoretical model of mars' neutral atmospheric composition between 30 and 200 km. *Journal of Geophysical Research: Solid Earth*, *95*(B9), 14795–14810.

Schreier, F., Milz, M., Buehler, S. A., & von Clarmann, T. (2018). Intercomparison of three microwave/infrared high resolution line-by-line radiative transfer codes. *Journal of Quantitative Spectroscopy and Radiative Transfer*, *211*, 64–77.

Shaposhnikov, D. S., Medvedev, A. S., Rodin, A. V., & Hartogh, P. (2019). Seasonal water pump in the atmosphere of mars: Vertical transport to the thermosphere. *Geophysical Research Letters*, *46*(8), 4161–4169.

Sindoni, G., Formisano, V., & Geminale, A. (2011). Observations of water vapour and carbon monoxide in the martian atmosphere with the swc of pfs/mex. *Planetary and Space Science*, *59*(2-3), 149–162.

Smith, M. D., Daerden, F., Neary, L., & Khayat, A. (2018). The climatology of carbon monoxide and water vapor on Mars as observed by CRISM and modeled by the gem-Mars general circulation model. *Icarus*, *301*, 117–131.

Smith, M. D., Daerden, F., Neary, L., Khayat, A. S., Holmes, J. A., Patel, M. R., ... others (2021). The climatology of carbon monoxide on Mars as observed by NOMAD nadir-geometry observations. *Icarus*, *362*, 114404.

Smith, M. D., Wolff, M. J., Clancy, R. T., & Murchie, S. L. (2009). Compact reconnaissance imaging spectrometer observations of water vapor and carbon monoxide. *Journal of Geophysical Research: Planets*, *114*(E2).

Sprague, A., Boynton, W., Kerry, K., Janes, D., Hunten, D., Kim, K., ... Metzger, A. (2004). Mars' south polar ar enhancement: A tracer for south polar seasonal meridional mixing. *Science*, *306*(5700), 1364–1367.

Stiller, G. P. (2000). The karlsruhe optimized and precise radiative transfer algo-

This article is protected by copyright. All rights reserved.

Accepted Article

21699100, ja, Downloaded from https://agupubs.onlinelibrary.wiley.com/doi/10.1029/2022JE007282 by The Open University, Wiley Online Library on [23/02/2023]. See the Terms and Conditions (https://onlinelibrary.wiley.com/terms-and-conditions) on Wiley Online Library for rules of use; OA articles are governed by the applicable Creative Commons License

rithm (KOPRA).

Stolzenbach, A., Lpez-Valverde, M.-A., Funke, B., Brines, A., Modak, A., Gonzlez-Galindo, F., ... Patel, M. (2022). Martian atmospheric aerosols composition and distribution retrievals during the 1st Martian year of NOMAD/TGO solar occultation measurements. *JGR-submitted*.

Streeter, P. M., Lewis, S. R., Patel, M. R., Holmes, J. A., Fedorova, A. A., Kass, D. M., & Kleinböhl, A. (2021). Asymmetric impacts on mars polar vortices from an equinoctial global dust storm. *Journal of Geophysical Research: Planets*, *126*(5), e2020JE006774.

Thomas, I., Vandaele, A., Robert, S., Neefs, E., Drummond, R., Daerden, F., ... others (2016). Optical and radiometric models of the NOMAD instrument part ii: the infrared channels-SO and LNO. *Optics Express*, *24*(4), 3790–3805.

Thomas, I. R., Aoki, S., Trompet, L., Robert, S., Depiesse, C., Willame, Y., ... others (2022). Calibration of nomad on esa's exomars trace gas orbiter: Part 1–the solar occultation channel. *Planetary and Space Science*, *218*, 105411.

Toigo, A., Waugh, D. W., & Guzewich, S. D. (2017). What causes mars' annular polar vortices? *Geophysical Research Letters*, *44*(1), 71–78.

Vandaele, A. C., Korablev, O., Daerden, F., Aoki, S., Thomas, I. R., Altieri, F., ... others (2019). Martian dust storm impact on atmospheric h2o and d/h observed by exomars trace gas orbiter. *Nature*, *568*(7753), 521–525.

Vandaele, A. C., Lopez-Moreno, J.-J., Patel, M. R., Bellucci, G., Daerden, F., Ristic, B., ... others (2018). NOMAD, an integrated suite of three spectrometers for the exoMars trace gas mission: Technical description, science objectives and expected performance. *Space Science Reviews*, *214*(5), 1–47.

Vandaele, A. C., Willame, Y., Depiesse, C., Thomas, I. R., Robert, S., Bolsée, D., ... others (2015). Optical and radiometric models of the NOMAD instrument part i: the UVIS channel. *Optics Express*, *23*(23), 30028–30042.

Villanueva, G. L., Liuzzi, G., Aoki, S., Stone, S. W., Brines, A., Thomas, I. R., ... others (2022). The deuterium isotopic ratio of water released from the martian caps as measured with tgo/nomad. *Geophysical Research Letters*, *49*(12), e2022GL098161.

Villanueva, G. L., Liuzzi, G., Crismani, M. M., Aoki, S., Vandaele, A. C., Daerden, F., ... others (2021). Water heavily fractionated as it ascends on mars as

This article is protected by copyright. All rights reserved.

Accepted Article

21699100, ja, Downloaded from https://agupubs.onlinelibrary.wiley.com/doi/10.1029/2022JE007282 by The Open University, Wiley Online Library on [23/02/2023]. See the Terms and Conditions (https://onlinelibrary.wiley.com/terms-and-conditions) on Wiley Online Library for rules of use; OA articles are governed by the applicable Creative Commons License

revealed by exomars/nomad. *Science Advances*, *7*(7), eabc8843.

von Clarmann, T., Glatthor, N., Grabowski, U., Hpfner, M., Kellmann, S., Kiefer, M., ... Lpez-Puertas, M. (2003). Retrieval of temperature and tangent altitude pointing from limb emission spectra recorded from space by the Michelson Interferometer for Passive Atmospheric Sounding (MIPAS). *Journal of Geophysical Research: Atmospheres*, *108*.

Yoshida, N., Nakagawa, H., Aoki, S., Erwin, J., Vandaele, A. C., Daerden, F., ... others (2022). Variations in vertical CO/CO2 profiles in the martian mesosphere and lower thermosphere measured by the exomars tgo/nomad: Implications of variations in eddy diffusion coefficient. *Geophysical Research Letters*, e2022GL098485.

This article is protected by copyright. All rights reserved.

Accepted Article

21699100, ja, Downloaded from https://agupubs.onlinelibrary.wiley.com/doi/10.1029/2022JE007282 by The Open University, Wiley Online Library on [23/02/2023]. See the Terms and Conditions (https://onlinelibrary.wiley.com/terms-and-conditions) on Wiley Online Library for rules of use; OA articles are governed by the applicable Creative Commons License